Numerical Simulations of Hypersonic Boundary Layer Transition

A DISSERTATION

SUBMITTED TO THE FACULTY OF THE GRADUATE SCHOOL

OF THE UNIVERSITY OF MINNESOTA

BY

Matthew David Bartkowicz

IN PARTIAL FULFILLMENT OF THE REQUIREMENTS

FOR THE DEGREE OF

Doctor of Philosophy

Professor Graham Candler

January, 2012

© Matthew David Bartkowicz 2012
ALL RIGHTS RESERVED

Acknowledgements

My advisor, Graham Candler, has been extremely encouraging and supportive. The enthusiasm he exudes and the fun he has with this research has been inspirational. This work would not have been possible without the many discussions and contributions from my colleagues. Mike Barnhardt, Travis Drayna, Heath Johnson, Ioannis Nompelis, Dave Peterson, Pramod Subbareddy and Ross Wagnild have all contributed to my success. My parents, Dave and Nancy, my brother Stefan, my sister Katie and the rest of my family have also been supportive of my never-ending collegiate career. I could not have achieved all I have without the support and encouragement of all these people.

To my beautiful fiancée and soon-to-be wife, Lindsay

Abstract

Numerical schemes for supersonic flows tend to use large amounts of artificial viscosity for stability. This tends to damp out the small scale structures in the flow. Recently some low-dissipation methods have been proposed which selectively eliminate the artificial viscosity in regions which do not require it. This work builds upon the low-dissipation method of Subbareddy and Candler which uses the flux vector splitting method of Steger and Warming but identifies the dissipation portion to eliminate it.

Computing accurate fluxes typically relies on large grid stencils or coupled linear systems that become computationally expensive to solve. Unstructured grids allow for CFD solutions to be obtained on complex geometries, unfortunately, it then becomes difficult to create a large stencil or the coupled linear system. Accurate solutions require grids that quickly become too large to be feasible. In this thesis a method is proposed to obtain more accurate solutions using relatively local data, making it suitable for unstructured grids composed of hexahedral elements. Fluxes are reconstructed using local gradients to extend the range of data used. The method is then validated on several test problems.

Simulations of boundary layer transition are then performed. An elliptic cone at Mach 8 is simulated based on an experiment at the Princeton Gasdynamics Laboratory. A simulated acoustic noise boundary condition is imposed to model the noisy conditions of the wind tunnel and the transitioning boundary layer observed. A computation of an isolated roughness element is done based on an experiment in Purdue's Mach 6 quiet wind tunnel. The mechanism for transition is identified as an instability in the upstream separation region and a comparison is made to experimental data. In the CFD a fully turbulent boundary layer is observed downstream.

Contents

List of Tables

List of Figures

Chapter 1

Introduction

1.1 Motivation and Objectives

Arguably the largest impediment to hypersonic flight is uncertainty in the state of the boundary layer. Skin friction as well as heat flux can increase by up to an order of magnitude if a hypersonic boundary layer transitions from laminar to turbulent. Though increased drag is not insignificant, the increased heat load can be especially catastrophic. Conservative designs are usually chosen which typically require more mass for the thermal protection system and, consequently, result in a smaller available payload mass budget. Clearly, then, it would be extremely useful to know what the state of the boundary layer will be during flight, or, even better, design the vehicle such that the desired state is achieved.

Transition typically happens in one of two ways. Natural transition occurs when disturbances present in the freestream, either from 'noisy' wind tunnels or fluctuations in the atmosphere, enter the boundary layer and grow. At high Mach number, the dominant instability is the second, or Mack, mode (Mack (1984)). This mode can be seen growing and causing transition in Figure 1.1, a shadowgraph taken from Hornung (2002).

Alternatively, the boundary layer can become turbulent due to roughness. Roughness is a generic term for surface irregularity and is somewhat vague. It can mean distributed roughness, such as an un-polished surface similar to sandpaper, or a single large roughness element, such as a bolt put in place for structural or mechanical reasons. Rather than freestream disturbances entering the boundary layer, disturbances are created by the roughness which can then find conditions suitable to grow and cause transition. Figure 1.2 is a nitric oxide (NO) planar laser-induced florescence (PLIF) image taken by Danehy (2010)

showing transition due a single, cylindrical roughness element. This clearly shows the disturbances being created by the roughness along with growth leading to breakdown of the boundary layer.

Actually, a combination of both freestream disturbances and some level of roughness is involved in the transition process.

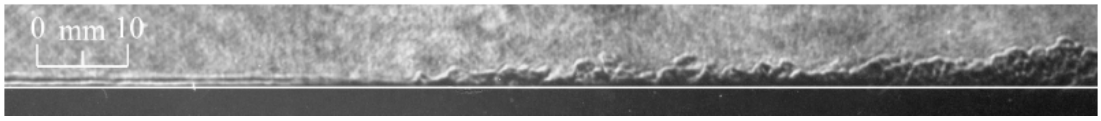

Figure 1.1: The picture above is taken from Hornung (2002). Nitrogen flow over a cone is transitioning from laminar to turbulent in the T5 hypervelocity shock tunnel.

To better understand the process of boundary layer transition, and eventually be able to predict with confidence whether said boundary layer will be laminar or turbulent, a combination of experiments and numerical simulations are needed. Unfortunately, many aspects of numerical methods used for high speed flows make the simulation of unsteady flows unsatisfactory. Shock capturing schemes, though sophisticated and very useful for supersonic flows, use large amounts of numerical viscosity to maintain stability. This, in turn, damps out small scale structures and unsteadiness.

Attempts at eliminating the numerical viscosity, except where needed for stability (shocks), have been largely successful (Yee et al. (1999) and Subbareddy and Candler (2009)). For most flux schemes it is relatively simple to separate out the numerical dissipation. In this thesis, which largely builds upon the work of Subbareddy and Candler (2009), the numerical dissipation is separated from the non-dissipative (though dispersive) part of the flux and 'turned off' in regions where it isn't needed.

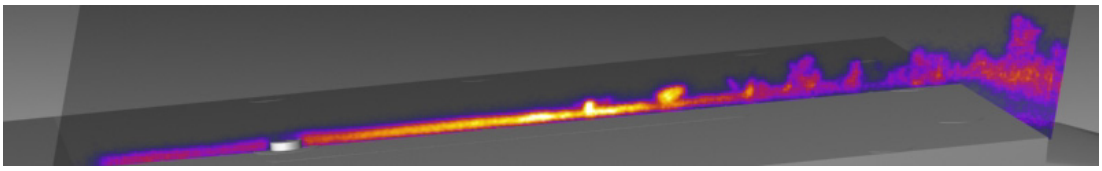

Figure 1.2: Shown above is an NO-PLIF image of a boundary layer transitioning in the 31 Inch Mach 10 Air Tunnel at NASA Langley Research Center (taken from Danehy (2010)).

As one would expect, removing the dissipation put in place for stability is only trading one difficulty for another; dispersion error, normally damped out by artificial viscosity, can

now become quite large. Obtaining more accurate solutions requires large stencils or a coupled system with large linear systems expensive to solve. In the past this was somewhat simpler to do because computational solvers used structured grids almost exclusively. As unstructured grids became more prevalent, due to their ability to handle more complex geometries and the relative simplicity of creating each grid, second order accuracy became the most achievable order of accuracy. However, having eliminated the numerical dissipation to allow for smaller scales to be resolved, it would be ideal if a higher (than second) order accurate base scheme could be achieved.

A grid can never resolve wavenumbers higher than the Nyquist limit, allowing for only moderate Reynolds numbers to be accessible to simulation until computational resources grow more powerful, it is the goal of this work to extend the limitation on Reynolds number as far as possible. By working in an unstructured framework, but still taking time to make well-designed grids, it should be possible to take advantage of both. The hope is that using stable, highly accurate low-dissipation schemes, the small scales associated with boundary layer transition can be simulated on complex geometries at realistic conditions. Below is an outline of the following work.

1.2 Chapter Summaries

- Chapter 2 presents the numerical method used in some detail. Also, a method for obtaining more accurate inviscid fluxes is put forth that made the work in this thesis possible.
- In Chapter 3 are a few validation problems which make clear the capability of this work.
- Chapter 4 presents simulations of natural transition on an elliptic cone due to acoustic disturbances in the freestream. The conditions correspond to experiments done at Princeton's Gasdynamics Laboratory.
- Chapter 5 contains results of roughness induced transition calculations. The geometry and condition correspond to experiments in Purdue's Mach 6 quiet wind tunnel.
- In Chapter 6 a final discussion is presented with conclusions.

Chapter 2

Numerical Method

2.1 Governing Equations

For a thermally and calorically perfect gas in which a continuum assumption is valid, the Navier-Stokes equations are a very good description for aerodynamic flows. In partial differential equation form they are:

$$\frac{\partial \rho}{\partial t} + \frac{\partial \rho u_i}{\partial x_i} = 0 \tag{2.1a}$$

$$\frac{\partial \rho u_i}{\partial t} + \frac{\partial}{\partial x_j}\left(\rho u_i u_j + p\delta_{ij} - \tau_{ij}\right) = 0 \tag{2.1b}$$

$$\frac{\partial E}{\partial t} + \frac{\partial}{\partial x_j}\left((E+p)u_j - \tau_{ij}u_i + q_j\right) = 0 \tag{2.1c}$$

The first equation is conservation of mass, the second is conservation of momentum in the i directions, and the last is conservation of energy. In these equations ρ is the fluid density. The fluid velocity is u_i (or equivalently u, v, w for $i = 1, 2, 3$). The pressure and total energy are p and E. The viscous stress, τ_{ij}, is proportional to the first derivatives of the velocity.

$$\tau_{ij} = \mu\left(\frac{\partial u_i}{\partial x_j} + \frac{\partial u_j}{\partial x_i}\right) + \lambda\frac{\partial u_k}{\partial x_k}\delta_{ij} \tag{2.2}$$

Sutherland's Law is used to determine the viscosity.

$$\mu(T) = \mu_o \frac{T^{\frac{3}{2}}}{T + T_o} \tag{2.3}$$

The constants for air are $\mu_o = 1.458 \times 10^{-6}\ kg/m\text{-}s$ and $T_o = 110.3$ K. λ is the second coefficient of viscosity and is typically assumed to be $\lambda = -\frac{2}{3}\mu$. The heat conduction is given by Fourier's law and is proportional to the temperature gradient.

$$q_j = -\kappa \frac{\partial T}{\partial x_j} \tag{2.4}$$

κ is related to the viscosity through the Prandtl number by $Pr = \frac{c_p \mu}{\kappa}$. For air under most conditions the Prandtl number is approximately 0.72.

For a calorically perfect gas the specific heats, c_v and c_p, are constant ($c_p = c_v + R$) and the specific internal energy varies linearly with the temperature: $e = c_v T$. If the gas is also thermally perfect the pressure is given by the ideal gas law, $p = \rho R T$, where R is the gas constant. The total energy, E, is the sum of the kinetic energy, $\frac{1}{2}\rho u_i u_i$, and the internal energy, $\rho c_v T$. This formulation of the governing equations is valid for compressible flow at supersonic, and even hypersonic, speeds as long as the temperatures reached remain below the point at which vibrational modes and chemical non-equilibrium need to be accounted for.

2.2 Finite Volume Formulation

The above Navier-Stokes equations are written in conservation, or divergence, form. It can be written more compactly as the following:

$$\frac{\partial U}{\partial t} + \frac{\partial F_i}{\partial x_i} = 0 \tag{2.5}$$

and

$$U = \begin{pmatrix} \rho \\ \rho u \\ \rho v \\ \rho w \\ E \end{pmatrix} \quad , \quad F_i = \begin{pmatrix} \rho u_i \\ \rho u u_i + p\delta_{1,i} - \tau_{1i} \\ \rho v u_i + p\delta_{2,i} - \tau_{2i} \\ \rho w u_i + p\delta_{3,i} - \tau_{3i} \\ (E+p)u_i - \tau_{ji} u_j + q_i \end{pmatrix} \tag{2.6}$$

Integrating over an arbitrary control volume with volume V and boundary ∂V, it is then possible to use Gauss' theorem to convert the volume integral to a surface integral over the boundary.

$$\int_V \frac{\partial U}{\partial t} = -\int_V \frac{\partial F_i}{\partial x_i} dV \xrightarrow[Theorem]{Gauss'} -\oint_{\partial V} F \cdot dS \tag{2.7}$$

The volume integral of the conserved variables changes due to the fluxes on the boundary; physically this makes sense and is why finite volume methods are so intuitive. Discretizing the right hand side of this equation so that each cell in the computational grid is the control volume results in the following semi-discrete equation.

$$V_i \frac{\partial U_i}{\partial t} = -\sum_f (F_f \cdot S) \tag{2.8}$$

In this equation the subscript i refers to an arbitrary grid cell and the subscript f refers to the faces of the polyhedron that make the boundary of cell i (Figure2.1). U_i is the volume average of U. Usually a single point quadrature is used and the flux for face f is evaluated at the face centroid. A variable with the prime symbol, such as F' or u', indicates a dot product with the unit normal of the face, $\hat{n}$, through which the flux is being evaluated. This is also called the rotated flux or rotated velocity. From this point on F and F' are used interchangeably to represent the rotated flux unless specifically noted. The cells in the vicinity of the face are then labeled based on this direction such that the face normal points from left to right. Left and right cells have the subscript L and R, respectively. If a larger stencil is known, the cells adjacent to the opposite face may be known as well – these are labeled with the subscript $L2$ and $R2$. This notation can become confusing as the subscripts L and R can also mean the reconstruction *from* the left or *from* the right. Thus a transformation to a one dimensional line is used instead: $(L2, L, R, R2) \rightarrow (i{-}1, i, i{+}1, i{+}2)$.

The equation to solve is the following,

$$\frac{\partial U_i}{\partial t} = -\frac{1}{V_i} \sum_f (F'_f S_f) \tag{2.9}$$

and the items left to determine are the time derivative and the evaluation of the fluxes.

2.3 Steger-Warming Flux Vector Splitting

When the viscous stress terms and heat conduction terms are dropped, what's left are the Euler equations containing only the convective and pressure terms. The Euler equations have a hyperbolic character, and for equations of this type information travels along characteristics. The terms that are dropped (the viscous stresses and the heat conduction) are elliptic in character and have much different solutions than the wave like solutions of hyperbolic systems. Because of this difference, the fluxes are often split in to an inviscid flux

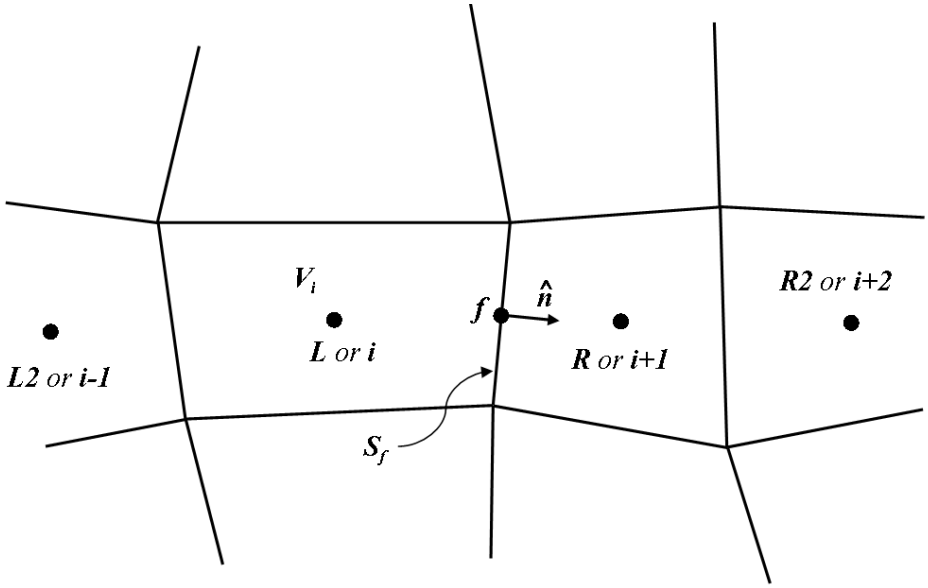

Figure 2.1: Shown is a schematic of an arbitrary quadrilateral grid in two dimensions. The computed flux at face f would use data from the cells to the left and right. The subscripts L and R can be used, but more often the grid is transformed to a one dimensional line and the subscript i is used instead.

and viscous flux,

$$F = F_{\mathrm{I}} + F_{\mathrm{V}} \tag{2.10}$$

which are treated in very different ways. The viscous fluxes use central difference schemes which tend to be fairly simple; more will be said about these in a later section.

The inviscid fluxes, on the other hand, need much more sophisticated methods to construct stable schemes. The flux vector-splitting method of Steger and Warming (1981) is employed in this work. This method, like other successful schemes, uses the wave like nature of the Euler equations as well as upwinding to capture shocks.

The fluxes in the Euler equations are homogeneous in the vector of conserved variables,

$$F(\lambda U) = \lambda F(U) \tag{2.11}$$

which means, by the Euler homogeneous function theorem, that the fluxes can be linearized with the flux Jacobian as the following:

$$F(U) = \frac{\partial F}{\partial U} U = AU \tag{2.12}$$

In this equation A is the inviscid flux Jacobian (also rotated into the face normal frame of reference).

The next step is to diagonalize A, but first a trick is employed to simplify the results. Transforming into the vector of primitive variables, $(\rho, u, v, w, p)^T$, and using the identity below it is possible to work with a more convenient set of variables and then transform back into conserved variables.

$$A = \frac{\partial F}{\partial U} = \frac{\partial U}{\partial V}\frac{\partial V}{\partial U}\frac{\partial F}{\partial V}\frac{\partial V}{\partial U} \tag{2.13}$$

Defining the transformation matrices as $S^{-1} = \frac{\partial U}{\partial V}$ and $S = \frac{\partial V}{\partial U}$ leaves the center matrix to diagonalize as $M = \frac{\partial F'}{\partial V}\frac{\partial V}{\partial U}$. This is easily done as:

$$M = C^{-1}\Lambda C \tag{2.14}$$

This may appear to be needlessly complicated, but in practice M is much easier to diagonalize than A. The matrices S^{-1}, C^{-1}, C and S are obtained by taking the appropriate derivatives and solving the eigenvalue problem. These matrices can be found in full elsewhere (Subbareddy (2007), for example). Λ is the diagonal matrix of eigenvalues.

At this point is where the flux splitting is done. Λ is split into positive and negative components as

$$\Lambda^{\pm} = \frac{\Lambda \pm |\Lambda|}{2} \tag{2.15}$$

Physically this corresponds to the waves traveling in the positive and negative directions and is the key for this method capturing the wave nature of the hyperbolic system.

The flux vector is split into the positive and negative parts based on the sign of the eigenvalues as well.

$$F = F^+ + F^- \tag{2.16}$$

Upwinding of the fluxes is done by evaluating the positive flux from upwinded data and the negative fluxes from downwind data (upwind from the negative moving information's point of view). The original Steger-Warming method does this the following way:

$$\begin{aligned} F_f^+ &= A^+(U_i)\cdot U_i \\ F_f^- &= A^-(U_{i+1})\cdot U_{i+1} \end{aligned} \tag{2.17}$$

A modification to this is typically used in the evaluation of the Jacobian (this modification is cleverly known as modified Steger-Warming). The Jacobians are evaluated at the

cell face f. Any reasonable average is acceptable. The fluxes then take the form

$$\begin{aligned} F_f'^{+} &= A^+(U_f)\cdot U_i \\ F_f'^{-} &= A^-(U_f)\cdot U_{i+1} \end{aligned} \tag{2.18}$$

Although not obvious in this form, numerical experiments show that the modified form has less dissipation and the difference is especially noticeable in boundary layers and shear layers. Another consequence of this is less stability at discontinuities. A combination of the two is used to combine the benefits of both. The state vector used to evaluate the Jacobian is a weighted average of the left and right states.

$$U_f = \alpha U_i + (1-\alpha)U_{i+1} \tag{2.19}$$

The parameter α is a switch, usually pressure based, that tends to zero or one at discontinuities to upwind the Jacobian, but limits to one half in smooth regions.

One more improvement to the original Steger-Warming fluxes is the so-called sonic glitch correction. This occurs in regions of the flow where the eigenvalues approach zero. As the name implies, it occurs at sonic lines where the eigenvalues $u' \pm a$ may be zero, but also in stagnation regions where the eigenvalues of u' are zero. Consider the case in which an eigenvalue at a face is zero. From the left the eigenvalue is positive and f^+, the flux for that characteristic, is non-zero. From the right the eigenvalue is negative and f^- is non-zero as well. This non-physical double counting of the characteristic can cause numerical error to develop. In stagnation regions this error will build up due to the lack of a mechanism to convect it away. The solution to this problem is to disallow any eigenvalues from becoming zero. This is typically done in the following way

$$\hat{\lambda}^{\pm} = \frac{\lambda^{\pm} \pm \sqrt{\lambda^{\pm 2} + \epsilon^2}}{2} \tag{2.20}$$

where ϵ is some small fraction of the speed of sound. The evaluation of the Jacobians use this modified eigenvalue.

2.3.1 Higher Order Spatial Accuracy

The fluxes for modified Steger-Warming are split and written as

$$\begin{aligned} F_f &= F^+ + F^- \\ &= A^+(U_f)\cdot U_i + A^-(U_f)\cdot U_{i+1} \end{aligned} \tag{2.21}$$

Multiplying the Jacobians by the state vectors, U, in cell i for the positive flux and $i+1$ for the negative flux is equivalent to a first order extrapolation from the cell centers to the face f. Instead, replace U_i and U_{i+1} with U_L and U_R. These are now higher order extrapolations to the face.

$$F_f = A^+(U_f) \cdot U_L + A^-(U_f) \cdot U_R \tag{2.22}$$

Increasing the order of accuracy has the obvious advantage of increasing the resolution of smaller scales. But for fluxes that are upwinded, such as the Steger-Warming fluxes outlined above, the added artificial viscosity damps out any small scales. For high Reynolds number flows (Reynolds number being the ratio of inviscid forces to viscous forces) the artificial viscosity is orders of magnitudes higher than the physical viscosity. Such high numerical damping will effectively change the Reynolds number. For this reason it is informative to split the flux into a central part, which contains no numerical dissipation, and the dissipative part resulting from the upwinding.

$$\begin{aligned} F_f &= \left(C^{-1}S^{-1}\Lambda^+ SC\right)_f \cdot U_L + \left(C^{-1}S^{-1}\Lambda^- SC\right)_f \cdot U_R \\ &= \left(C^{-1}S^{-1}\tfrac{\Lambda+|\Lambda|}{2}SC\right)_f \cdot U_L + \left(C^{-1}S^{-1}\tfrac{\Lambda-|\Lambda|}{2}SC\right)_f \cdot U_R \\ &= \left(C^{-1}S^{-1}\Lambda SC\right)_f \cdot \tfrac{U_L+U_R}{2} - \tfrac{1}{2}\left(C^{-1}S^{-1}|\Lambda|SC\right)_f \cdot (U_R - U_L) \\ &= \underbrace{A \cdot \left(\frac{U_L+U_R}{2}\right)}_{central} \underbrace{-\frac{1}{2}|A| \cdot (U_R - U_L)}_{upwinded/dissipative} \end{aligned} \tag{2.23}$$

The equations naturally split into a symmetric term with the average of the left and right states and another term which contains the difference between the right and left states. This second term makes apparent the reason why upwinding adds artificial viscosity – the difference between the right and left states is like a difference, or first derivative, across the face. Recall that the viscous fluxes are proportional to first derivatives of the primitive variables; thus the upwinding creates terms that numerically look like viscosity.

The central term is treated differently from the upwinded term and will be considered in a moment.

Turning first to the dissipative portion of the flux there are a few things to note. First, the Jacobian is formally second order, using only data from i and $i+1$. Increasing the order of accuracy of U_L and U_R won't change this term (this is one of the reasons the central term is treated differently). However, this can be considered simply a constant multiplier

in front of the difference across the face.

The term that changes with different reconstructions to the face is $(U_R - U_L)$. First, this term is a difference across the face or a first derivative. This is why the term appears as dissipation. The difference across the face for first order upwind, second order upwind and third order upwind biased reconstructions is the following:

$$\begin{aligned}(U_R - U_L)_{1^{st}} &= U_{i+1} - U_i \\ (U_R - U_L)_{2^{nd}} &= \tfrac{1}{2}(U_{i-1} - 3U_i + 3U_{i+1} - U_{i+2}) \\ (U_R - U_L)_{3^{rd}} &= \tfrac{1}{8}(U_{i-1} - 3U_i + 3U_{i+1} - U_{i+2})\end{aligned} \tag{2.24}$$

Note that the first order extrapolation gives a difference proportional to the first derivative times the grid spacing while the second and third order extrapolations give a difference proportional to the third derivative times the grid spacing cubed. And also, the second and third order schemes give identical results except for the factor of four. Simply by reducing the dissipation level the range of scales that can be resolved in the flow improves significantly.

Taking this to the logical conclusion, it seems reasonable to reduce the numerical dissipation completely in regions where it isn't need for stability. Looking again at the flux that has been split into a central and dissipative upwinded part, multiplying the upwinded term by a factor, α, can accomplish this.

$$F = F_{\mathrm{C}} + \alpha F_{\mathrm{D}} \tag{2.25}$$

The factor α is somewhat arbitrary, but must be able to detect regions of the flow in which dissipation is needed. A useful switch was put forth by Ducros (1999) which uses the dilatation to vorticity ratio; this switch is based on the physics of the flow which is satisfying intuitively.

$$\alpha = \frac{\theta^2}{\theta^2 + \omega^2 + \epsilon} \tag{2.26}$$

The divergence and vorticity are θ and ω, respectively, and ϵ is a small number.

Another switch, put forth by Ren (2003), is more mathematical and simply looks for large changes in the solution. The choice of switches is somewhat problem dependent and must be explored in each case. The Ren switch uses characteristic variables, though when

employed in this work the density is used instead.

$$\alpha = \max(\hat{\rho}_i, \hat{\rho}_{i+1}) \quad , \quad \hat{\rho}_i = 1 - \frac{2|\Delta\rho_{i+1/2}\ \Delta\rho_{i-1/2}| + \epsilon}{\Delta\rho^2_{i+1/2} + \Delta\rho^2_{i-1/2} + \epsilon} \tag{2.27}$$

Where ϵ is a small number and $\Delta\rho_{i+1/2} = \rho_{i+1} - \rho_i$.

In this way the dissipation is only used in locations in the flow where it is absolutely needed and the flow physics are more accurately captured.

Now that the numerical dissipation has been addressed, the central portion of the flux needs some attention. In order to get higher order accuracy, the Jacobians are no longer used as they are inherently second order. Instead the flux is computed directly from a weighted average of data to the left and right. Now, to get a larger stencil despite the grid being unstructured an obvious idea is to use gradients and extrapolate to the face. For example, $\phi_f = \phi_i + \nabla\phi_i \cdot \Delta x$ would be an extrapolation from the left. A similar extrapolation from the right and then averaging the two would yield a larger stencil. It seems it would be more accurate, would it be higher *order* accurate? The answer to that question is most easily found on a one dimensional stencil. Using the known result of the gradient calculation in the left and right cells (Section 2.4 below) it is possible to find the optimal coefficient to put in front of the gradient term in the extrapolation to get the correct stencil weights.

$$\phi_f = \frac{\phi_i + \phi_{i+1}}{2} + \beta\left(\left.\frac{df}{dx}\right|_i \Delta x_i + \left.\frac{df}{dx}\right|_{i+1} \Delta x_{i+1}\right) \tag{2.28}$$

In this case the factor $\beta = 1/4$ obtains a fourth order interpolation at the face and the factor $\beta = 1/3$ obtains a fourth order gradient of the flux at the cell center after integrating over the surface of the cell. (Also note the Δx terms are the signed vectors from the cell center to the face center.)

If the gradients are computed using the Gauss-Green theorem then a surface integral is done for each cell. The extrapolation method just described can be used to compute more accurate gradients and can be done iteratively. Using gradients to to get better approximations for the surface integral allows for computing more accurate gradients. This process can be repeated and the stencil will continuously grow. Also important to note is that this method only requires very local data – useful for unstructured grids. The coefficients multiplying the gradient terms form a simple series that is only a function of the iteration number and total number of iterations to be done. Given below are the series

for both high order interpolations as well as interpolations which give high order gradients in the cell center. Note that the latter is correct for the inviscid fluxes, in which the quantity of interest is the gradient of the flux.

$$\begin{cases} \beta(j,n) = \frac{2(n-j)+1}{4(n-j)+4} & : \ n^{th} \text{ order interpolation} \\ \beta(j,n) = \frac{n-j+1}{2(n-j)+3} & : \ n^{th} \text{ order gradient} \end{cases} \tag{2.29}$$

Where n is the total number of iterations to compute (it must be decided upon beforehand) and j is the current iteration number.

Unfortunately, this relation only holds for grids that have even spacing. Further, boundary conditions reduce the order of accuracy near the boundary with the exception of periodic boundary conditions. In the case of even spacing with periodic boundary conditions Fourier methods may be a better choice. The only advantage the current method may have over the Fourier methods is computational cost. Fourier methods have $\mathcal{O}(N \log N)$ operations (with N points) while the current method has $\mathcal{O}(NM)$ operations with the chosen accuracy of M^{th} order. If $\mathcal{O}(M) < \mathcal{O}(\log N)$ then the current method will be less expensive (i.e. large numbers of points or relatively low order of accuracy).

If a hexahedral grid is assumed (which can still be unstructured) it is possible to imagine taking a linear combination of extrapolations from a larger stencil. What is meant by this is the following:

$$\begin{aligned} \phi_f = \tfrac{\phi_i+\phi_{i+1}}{2} \quad &+ \quad \beta\left(\left.\tfrac{df}{dx}\right|_i \Delta x_i + \left.\tfrac{df}{dx}\right|_{i+1} \Delta x_{i+1}\right) \\ &+ \quad \gamma\left(\left.\tfrac{df}{dx}\right|_{i-1} \Delta x_{i-1} + \left.\tfrac{df}{dx}\right|_{i+2} \Delta x_{i+2}\right) \end{aligned} \tag{2.30}$$

It can be easily verified that to obtain a sixth order stencil, the weights to be chosen are $\beta = 8/15$ and $\gamma = -1/45$.

This work uses gradients from nearby neighbors and either the fourth or sixth order inviscid fluxes computed via gradient reconstruction. It should be noted that the method has been derived for a one-dimensional stencil with equal spacing, yet it is still used on complex geometries with anisotropies in the grid. Though no longer formally of higher order in those cases, the method does prove to be more accurate and in fact vital to the ability to simulate flows that would otherwise require much larger grids. A qualitative example of the differences in the accuracy for non-uniform, three dimensional grids is presented in Chapter 3.

2.4 Viscous Fluxes

Computing the viscous fluxes is much simpler than the inviscid fluxes. It does, however, require computing gradients as all the fluxes are proportional to first derivatives of the primitive variables. Fluxes are computed at the face, but gradients are obtained at the cell center using one of two methods for unstructured grids. The steps for computing the fluxes are:

- Compute cell centered gradients
- From cell gradients, compute face centered gradients
- From face gradients, compute viscous fluxes

There are two commonly used methods for computing cell centered gradients on an unstructured grid. The first is using Gauss' theorem which relates the average gradient in the cell to an integral over the surface of the cell.

$$\frac{\partial \phi}{\partial x_i} = \frac{1}{V} \sum_f \phi \cdot \hat{n_i} \; S_f \tag{2.31}$$

Where ϕ is any variable for which a gradient is desired, V is the cell volume, $\hat{n}_i$ is the component of the unit surface normal in the direction of the gradient being computed and S_f is the face area. Notice the similarity to the calculation of the divergence of the fluxes to find the rate of change of the solution in the governing equation. This method works well for isotropic cells, but suffers in cells with high aspect ratio. (In general, a length scale is obtained for each face of a cell when cell volume is divided by face area. A very large or very small ratio of any two face's length scales indicates a large aspect ratio for this cell.) In high speed flows the cells near walls have much shorter length scales in the wall normal direction to resolve the boundary layer. Because of this, a weighted least squares method is more often used.

For least squares, consider a Taylor expansion about cell i to get the value at cell k. Subscript x and y indicate partial derivatives. This is done in two dimensions for brevity, though the extension to three dimensions is straight forward.

$$\phi_k = \phi_i + \phi_{x,i} \Delta x_{ik} + \phi_{y,i} \Delta y_{ik} + \mathcal{O}(\Delta x^2, \Delta y^2, \Delta x \Delta y) \tag{2.32}$$

Defining $d\phi$ as

$$d\phi_{ik} = \phi_k - \phi_i = \phi_{x,i}\Delta x_{ik} + \phi_{y,i}\Delta y_{ik} + \mathcal{O}(\Delta x^2, \Delta y^2, \Delta x \Delta y) \tag{2.33}$$

then the difference between $d\phi_{ik}$ and the gradient terms is the error of this approximation. The goal is to simultaneously minimize the square of this error (least square error) for every neighboring cell.

$$E_{ik}^2 = (d\phi_{ik} - \phi_x \Delta x_{ik} - \phi_y \Delta y_{ik})^2 \tag{2.34}$$

This is done by summing over the neighbors, k, taking derivatives with respect to each gradients and then setting each result equal to zero.

$$\begin{cases} \frac{\partial}{\partial \phi_{x,i}} \sum\limits_k w_{ik}^2 (d\phi_{ik} - \phi_{x,i}\Delta x_{ik} - \phi_{y,i}\Delta y_{ik})^2 = 0 \\ \frac{\partial}{\partial \phi_{y,i}} \sum\limits_k w_{ik}^2 (d\phi_{ik} - \phi_{y,i}\Delta x_{ik} - \phi_{y,i}\Delta y_{ik})^2 = 0 \end{cases} \tag{2.35}$$

After taking the derivatives and rearranging the terms the following is the result.

$$\begin{aligned} \overbrace{\sum_k w_{ik}^2 \Delta x_{ik}^2}^{a} \phi_x + \overbrace{\sum_k w_{ik}^2 \Delta x_{ik}\Delta y_{ik}}^{b} \phi_y &= \overbrace{\sum_k w_{ik}^2 \Delta x_{ik} d\phi_{ik}}^{d} \\ \underbrace{\sum_k w_{ik}^2 \Delta x_{ik}\Delta y_{ik}}_{b} \phi_x + \underbrace{\sum_k w_{ik}^2 \Delta y_{ik}^2}_{c} \phi_y &= \underbrace{\sum_k w_{ik}^2 \Delta y_{ik} d\phi_{ik}}_{e} \end{aligned} \tag{2.36}$$

The w terms are the weights assigned between cells. The solution to this system is the solution to the matrix equation.

$$\begin{pmatrix} \phi_x \\ \phi_y \end{pmatrix} = \frac{1}{ac - b^2} \begin{pmatrix} c & -b \\ -b & a \end{pmatrix} \begin{pmatrix} d \\ e \end{pmatrix} \tag{2.37}$$

At this point it is useful to point out a few things about this equation. The matrix, which is really the inverse of the left hand side of equation 2.36, depends only on the geometry of the grid (and the weights). For a static grid this can be computed once and stored. Only the vector containing d and e needs to be recomputed. Also, the denominator contains the term $(ac - b^2)$. If the weights are taken to be one this is order Δx^4, which for very small grid spacings may cause the system to be ill-conditioned. If the weight is instead chosen to be proportional to $1/\Delta x$ the denominator becomes order one and the system will be much better conditioned. However, numerical stability isn't the only consideration.

Consider for a moment the one dimensional case with constant grid spacing. Equation 2.37 reduces to

$$\phi_{x,i} = \frac{w_{i+1}^2\phi_{i+1} + (w_{i-1}^2 - w_{i+1}^2)\phi_i - w_{i-1}^2\phi_{i-1}}{(w_{i+1}^2 + w_{i-1}^2)\Delta x} \tag{2.38}$$

while a second order approximation to the gradient is

$$\phi_{x,i} = \frac{\phi_{i+1} - \phi_{i-1}}{2\Delta x} \tag{2.39}$$

It immediately follows that any weighting function that is a function of the grid only (not dependent on the solution) will result in a second order gradient. Using the inverse distance in this case would both result in second order accuracy and maintain numerical stability.

Now consider the one dimensional case in which the grid is growing by a constant growth factor of α. This is analogous to the stretching used in boundary layers. In this situation the formally second order approximation is instead

$$\phi_{x,i} = \frac{\phi_{i+1} + (\alpha^2 - 1)\ \phi_i - \alpha^2\ \phi_{i-1}}{\alpha(\alpha + 1)\Delta x} \tag{2.40}$$

and the weighted least squares approximation is

$$\phi_{x,i} = \frac{\alpha w_{i+1}^2\phi_{i+1} + (w_{i-1}^2 - \alpha w_{i+1}^2)\phi_i - w_{i-1}^2\phi_{i-1}}{(w_{i+1}^2 + \alpha^2 w_{i-1}^2)\Delta x} \tag{2.41}$$

Equating coefficients again gives three equations, with the following solution.

$$w_{i-1} = \alpha^{\frac{3}{2}} w_{i+1} \tag{2.42}$$

This is satisfied if the weight is proportional to $\Delta x^{-3/2}$, which still ensures that the method is second order accurate on evenly spaced grids ($\alpha = 1$), but is also second order accurate on stretched meshes. One possible downside is that the system may be ill-conditioned, however, in practice it seems to affect stability only slightly, if at all.

To obtain the gradient at the face, rather than the cell center, deferred correction is used. The reason for this being that simply averaging to the face from cell left and right gives a poor approximation to the gradient in the direction normal to the face. Rather, the compact approximation of the difference between the right and left states is used for that component while an average of left and right is used for components parallel to the face. If

$\hat{e}$ is the unit vector pointing from the cell center on the left to the cell center on the right and d is the distance between them, then the gradient at the face is

$$\nabla\phi_f = \frac{\nabla\phi_i + \nabla\phi_{i+1}}{2} + \left(\frac{\phi_{i+1} - \phi_i}{d} - \frac{\nabla\phi_i + \nabla\phi_{i+1}}{2} \cdot \hat{e}\right)\hat{e} \tag{2.43}$$

Though taking the average without the deferred correction will still yield a second order accurate stencil, it gives a very poor gradient approximation.

An advantage of using deferred correction is that it is very compact. Adding the gradient terms utilizes a larger stencil, which is typically considered a good thing; however, using the gradients from cell centers is less local and results in poorer accuracy. The issue in this case is incorrectly using this larger stencil, but a combination of averaging and deferred correction should make it possible to appropriately utilize it.

This method was not used in the work here, partly because focus was put on the inviscid fluxes. This was justified because the Reynolds numbers were high enough that the inertial forces dwarfed the viscous forces. However, high Reynolds number flows, especially shear flows, can have regions where the viscous fluxes become important. The extension of the gradient extrapolation for inviscid fluxes is therefore put in Appendix A.

Finally, for implicit time integration (to be discussed in the next section) viscous Jacobians are also need. The viscous Jacobians can be found elsewhere.

2.5 Time Integration

2.5.1 Explicit Time Integration

Having computed the surface integral (the right hand side) of the governing equations, it is now possible to march the solution in time. Most would agree that the simplest method is a first order explicit Euler method. Adopting a superscript n to indicate the time level of the solution, explicit Euler uses data at the n level to update the solution to the $n+1$ level.

$$U_i^{n+1} = U_i^n - \frac{\Delta t}{V_i}\sum_f (F_f^n S_f) \tag{2.44}$$

Though not possible to analyze the full nonlinear problem, Von Neumann analysis of the linear problem shows that this scheme is only stable for time steps of

$$\Delta t \leq \frac{\Delta x}{|u'| + c} \tag{2.45}$$

with c being the local speed of sound. This equation says that propagating information further than one cell per time step becomes unstable. The ratio of the time step taken to this explicit time step is known as the Courant number or the Courant-Fredericks-Lewy number (CFL) and for explicit Euler the maximum time step allowed is a CFL of one.

Other commonly used explicit schemes are the Runge-Kutta multi-stage explicit schemes. By evaluating the fluxes multiple times and after each time evolving the solution to a new stage, a higher order of accuracy in time can be achieved. Defining an operator, $L^{(n)}$, that is the surface integral of the fluxes at stage n as

$$L_i^{(n)} = -\frac{\Delta t}{V_i} \sum_f (F_f^n S_f) \tag{2.46}$$

then the explicit Euler method can more succinctly be written as

$$U_i^{n+1} = U_i^n + L_i^{(n)} \tag{2.47}$$

A two stage, second order accurate in time, Runge-Kutta method (RK2) can then be written as

$$\begin{aligned} U_i^1 &= U_i^n + L_i^{(n)} \\ U_i^{n+1} &= \tfrac{1}{2} U_i^n + \tfrac{1}{2} U_i^1 + \tfrac{1}{2} L_i^{(1)} \end{aligned} \tag{2.48}$$

For a three stage, third order accurate scheme (RK3) a free parameter is available. A commonly chosen scheme then is the TVD RK3 method of Gottlieb and Shu (1998). (TVD, or total variation diminishing, is a property of certain discretizations that essentially prevents any spurious oscillations from forming.)

$$\begin{aligned} U_i^1 &= U_i^n + L_i^{(n)} \\ U_i^2 &= \tfrac{3}{4} U_i^n + \tfrac{1}{4} U_i^1 + \tfrac{1}{4} L_i^{(1)} \\ U_i^{n+1} &= \tfrac{1}{3} U_i^n + \tfrac{2}{3} U_i^2 + \tfrac{2}{3} L_i^{(2)} \end{aligned} \tag{2.49}$$

these RK schemes are higher order accurate in time. However they require twice or thrice the number of computations for the extra flux evaluations at each time step.

2.5.2 Implicit Time Integration

In order to be able to take larger time steps, an implicit method must be used by evaluating the fluxes at the $n+1$ time level. Of course the solution isn't yet known at that time level, so the fluxes must be linearized and a coupled system solved. Linearizing the fluxes is relatively simple for the inviscid fluxes because the Jacobians have already been computed to obtain the dissipative portion of the flux. The linearized flux is also split using the split Jacobians. (The viscous fluxes must also be linearized which can be found elsewhere.)

$$\begin{aligned} F_f^{n+1} &= F_f^n + \underbrace{\left.\frac{\partial F}{\partial U}\right|_f^n \overbrace{(U_f^{n+1} - U_f^n)}^{\delta U_f^n}}_{\delta F_f^n} + \mathcal{O}(\Delta t^2) \\ &= F_f^n + A_f^n \delta U_f^n \\ &= F_f^n + A_f^{+n}\delta U_i^n + A_f^{-n}\delta U_{i+1}^n \\ &= F_f^n + \delta F_f^{+n} + \delta F_f^{-n} \end{aligned} \tag{2.50}$$

Now, using the linearized flux the equation to be solved is the following:

$$\delta U_i^n = L_i^{(n)} - \frac{\Delta t}{V_i}\sum_f (A_f^{+n}\delta U_i^n + A_f^{-n}\delta U_{i+1}^n) S_f \tag{2.51}$$

The subscript $i+1$ always refers to the cell sharing face f with cell i.

The equation is now fully coupled – meaning the solution requires an inversion of a large matrix. However, the equation for cell i only has terms from itself and its nearest neighbors, so the vast majority of the operator acting on the δU vector is zeroes. Nevertheless, it can be solved with either brute force or a sparse matrix solver. Another way to solve this system, cheaper in terms of computational cost and memory, is with relaxation sweeps. Writing the system as

$$\left(I + \frac{\Delta t}{V_i}\sum_f A_f^{+n} S_f\right)\delta U_i^n + \frac{\Delta t}{V_i}\sum_f A_f^{-n} S_f \delta U_{i+1}^n = L_i^{(n)} \tag{2.52}$$

it is possible to then move the δU terms that are not at i to the right hand side and introduce k as a superscript representing a sub-iteration. The method becomes the following.

for $k = 1 \rightarrow k_{max}$ **do**

$$\delta U_i^k = \left[I + \tfrac{\Delta t}{V_i}\sum_f A_f^{+n} S_f\right]^{-1}\left[L_i^{(n)} - \tfrac{\Delta t}{V_i}\sum_f A_f^{-n} S_f \delta U_{i+1}^{k-1}\right]$$

end for

$\delta U_i^n = \delta U_i^{k_{max}}$

Where k_{max} is a specified number of iterations. Alternatively, the loop could be set to continue the k iterations until the system converges to some tolerance, however in practice a value of four is typically used for k_{max}.

This is a point relaxation method and only involves matrices of size 5×5. Implementing this method is relatively simple which tends to make up for any inefficiencies it has as compared to a more direct solve of the full system.

To obtain higher order accuracy in time, two methods are used. The first is a second order backward difference for the discretization of the time derivative. Assuming a constant time step, it takes the following form.

$$\left.\frac{\partial U}{\partial t}\right|_i = \frac{3U_i^{n+1} - 4U_i^n + U_i^{n-1}}{2\Delta t} \tag{2.53}$$

After some rearrangement, a term shows up on the right hand side that contains the change in the solution from one time step previously. From this point, everything proceeds as before.

$$\delta U_i^n = -\frac{2\Delta t}{3V_i} \sum_f F_f^{n+1} \cdot S_f + \frac{1}{3}\delta U_i^{n+1} \tag{2.54}$$

The second method is a second order Crank-Nicolson scheme. It is useful because it has half the numerical dissipation associated with first order implicit Euler. In this scheme the fluxes are taken as an average of those evaluated at the n time level and those at the $n+1$ time level. This is slightly unstable, so based on the local CFL a small number, ϵ, is added to bias the fluxes slightly towards the $n+1$ level. However, due to the linearization of the fluxes to get the value at the $n+1$ level, this results in simply multiplying the Jacobians by some factor between one half and one.

$$\begin{aligned} F &= \left(\tfrac{1}{2} - \epsilon\right) F^n + \left(\tfrac{1}{2} + \epsilon\right) F^{n+1} \\ &= F^n + (\tfrac{1}{2} + \epsilon)\delta F \\ &= F^n + (\tfrac{1}{2} + \epsilon)(A^+ \delta U_i + A^- \delta U_{i+1}) \end{aligned} \tag{2.55}$$

The value of ϵ is problem dependent, but for the problems in this work it varies between 10^{-6} and 0.1 based on local CFL.

These second order time integration schemes can introduce some dispersion into the solution, however, it was found that for adequate spatial resolution the dispersion is negligible.

2.6 Boundary Conditions

Explicit boundary conditions are relatively straightforward. Ghost cells are assumed to exist adjacent to boundary cells and values are given to the fluid in this ghost cell such that the proper boundary value is obtained. For example, the inviscid wall boundary condition sets the ghost values to force the flow at the wall to be tangent:

$$\vec{u} \cdot \hat{n} = 0 \tag{2.56}$$

This is a reflection of the vector across the face. The average of the vector with its reflection results in a projection, which is necessarily parallel to the face.

Inflow boundaries are fully specified, either with freestream conditions or with a specified boundary layer profile (or any other profile). A time varying inflow can also be specified, such as a freestream with acoustic noise. Outflow boundaries typically use extrapolated data from the interior. In the case where the flow is supersonic the issue is somewhat irrelevant, as there are no characteristics running upstream. If the flow is subsonic, such as in the boundary layer where the wall meets the outflow, it can cause some problems. In those cases something else must be done, such as a sponge layer or a characteristic boundary condition. In the work presented here, care is taken with the geometry so that no special boundary condition is needed.

Viscous wall conditions are also rather trivial. The velocity in the ghost cell is the negative of the adjacent interior cell, enforcing the zero velocity ('no-slip') condition. The pressure is assumed to be constant through the boundary layer, $p_{ghost} = p_{interior}$, and an adiabatic wall has a similar temperature boundary condition, $T_{ghost} = T_{interior}$. For an isothermal wall of T_w the ghost cell is set such that the average of the two gives the wall temperature: $T_{ghost} = 2T_w - T_{interior}$.

Implicit boundary conditions are slightly more complicated and will only be briefly described here. The difficulty arises due to the δU_{i+1} terms in which $i+1$ refers to a ghost

cell. In this cell the solution is not updated, it is set from the interior values. Therefore it makes sense to fold it into the equation as a function of the interior. Consider the term $(A_f^-\ S_f\ \delta U_{i+1})$. As long as the ghost cell is a linear function of the interior cell, the state of the ghost cell can be written as some matrix operating on the state in the interior.

$$V_{ghost} = R\ V_{interior} \tag{2.57}$$

The primitive vector V is chosen because those variables have the imposed conditions, not the mass, momentum or energy. One could say that no mass is allowed to flow through the wall, but this is ultimately stating that the velocity is parallel to the face (inviscidly) or zero (viscous no-slip condition). It is the velocity which has the imposed condition. R is essentially a rotation matrix. It follows that the same relation holds for the change in the state:

$$\delta V_{ghost} = R\ \delta V_{interior} \tag{2.58}$$

Then, using the matrices discussed in section 2.3, it is easy to convert to conserved variables.

$$\delta U_{ghost} = S_{ghost}^{-1}\ R\ S_{interior} \delta U_{interior} \tag{2.59}$$

The implicit part of the flux for a boundary face then changes in the following way:

$$A_f^+\ S_f \delta U_i + A_f^-\ S_f\ \delta U_{i+1} = \left(A_f^+ + A_f^-\ S_{ghost}^{-1}\ R\ S_{interior}\right) S_f\ \delta U_i \tag{2.60}$$

In this way the implicit boundary condition is folded into the equation for the interior cell.

Chapter 3

Validation

Several problems are presented to display the advantage and capability of using the methods layed out in the last chapter. All simulations are conducted using US3D, an unstructured code developed at the University of Minnesota in which the higher order fluxes and time integration have been implemented. It is written in FORTRAN and fully parallel using MPI.

3.1 Convecting Density Pulse

The first problem is designed to test the accuracy of the inviscid fluxes using gradient reconstruction. A Gaussian pulse in density is initialized in a constant velocity, constant pressure field. The viscous fluxes have been discarded leaving only the Euler equations to be solved. This wave equation has a known solution at any time, t.

The domain is a one-dimensional, evenly spaced grid with periodic boundary conditions at the domain boundaries. The initial conditions are as follows:

$$\begin{cases} \rho(x,t_o) &= 1+\frac{1}{10}exp\left(-5\times 10^2 \ \left[\frac{x}{L}-\frac{1}{2}\right]^2\right) \\ u &= 1 \\ p &= 1 \end{cases} \tag{3.1}$$

where L is the domain length. This initial condition is a sharp Gaussian pulse in density in the center of the domain. It is known that at any later time, t, the pulse in density will simply move a distance $\Delta x = u\Delta t$ and the solution will be the following.

$$\rho(x,t) = \rho(x-u[t-t_o],t_o) \tag{3.2}$$

The solution is integrated in time with RK3 until the pulse travels a distance of L and returns to its original position (due to the periodic boundary condition). This was done

using a second order TVD MUSCL scheme (a common method of extrapolating the fluxes to obtain higher order without introducing spurious oscillations) as well as the second, fourth and sixth order schemes using gradient reconstruction. Numerical dissipation is not included because the flow is smooth and the time step is small (CFL= 0.1) so any errors can be attributed to the inviscid fluxes.

First, a qualitative assessment shows that all low-dissipation solutions have a much higher main peak in the pulse than even a 'higher-order' Steger-Warming flux method (Figure 3.1). Because a Gaussian pulse contains a wave number distribution which is also Gaussian, the dispersive error – error in the wave speed – causes the different wavenumbers comprising the pulse to separate. This appears in the solution as oscillations 'trailing' the main peak. However, even the difference between second and fourth order is vast in terms of reduction of this dispersion. The sixth order solution has almost no visible dispersion error for this problem.

Looking at the solution quantitatively, the reduction in error as the number of points is increased should correspond to the order of accuracy. As long as the time step is small enough so that the error corresponding to time integration is much smaller than the error associated with the fluxes, then the reduction in error should have a slope corresponding to the order of the fluxes. In Figure 3.2 the error can clearly be seen to follow this trend, as it should if the fluxes are higher order. This proof that the gradient extrapolation truly is higher order accurate is very satisfying. The next question is: How will the method perform in the presence of strong shocks?

3.2 Viscous Shock Tube

In this test problem the Navier-Stokes equations are employed rather than the Euler equations. A gas is initially separated by a thin membrane. The flow is at rest in both states, but initially the pressure and density on the left and right sides are:

$$\begin{pmatrix} \rho_L \\ p_L \end{pmatrix} = \begin{pmatrix} 120 \\ 120/\gamma \end{pmatrix} \quad , \quad \begin{pmatrix} \rho_R \\ p_R \end{pmatrix} = \begin{pmatrix} 1.2 \\ 1.2/\gamma \end{pmatrix} \tag{3.3}$$

Where γ is the ratio of specific heats and is $\frac{7}{5}$ for a diatomic gas. The domain is two dimensional in the range $0 \leq x \leq 1$ and $0 \leq y \leq 0.5$. The membrane is located at $x = 0$.

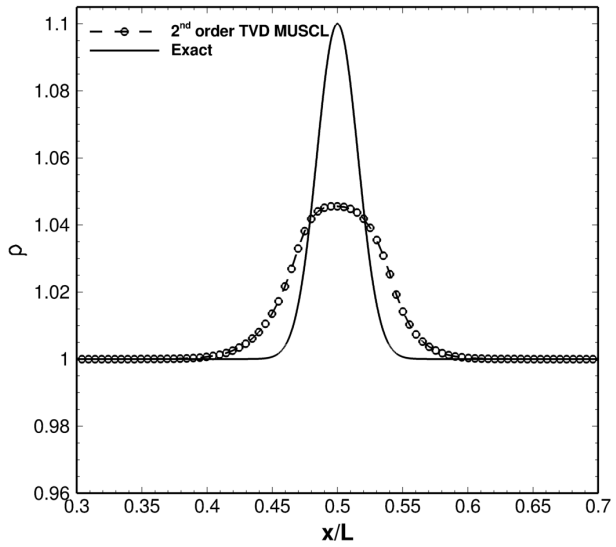

(a) Density profiles for 2^{nd} order TVD MUSCL and the exact solution.

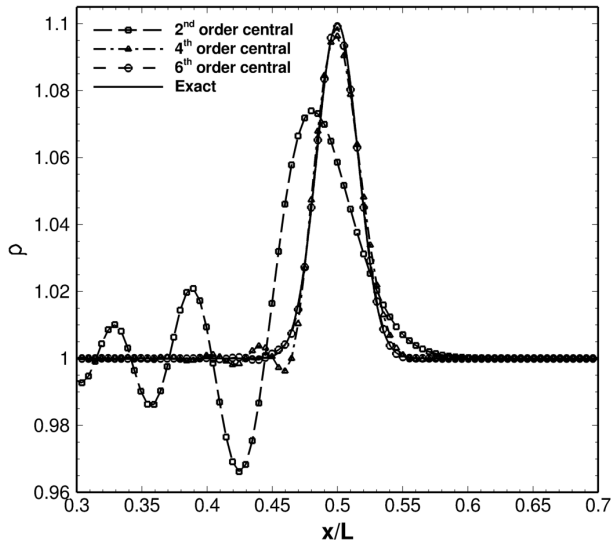

(b) Density profiles for 2^{nd}, 4^{th} and 6^{th} order central as well as the exact solution.

Figure 3.1: Figure 3.1(a) shows the level of dissipation for the standard fluxes. Figure 3.1(b) shows the difference between dissipation and dispersion as well as the difference between the flux methods.

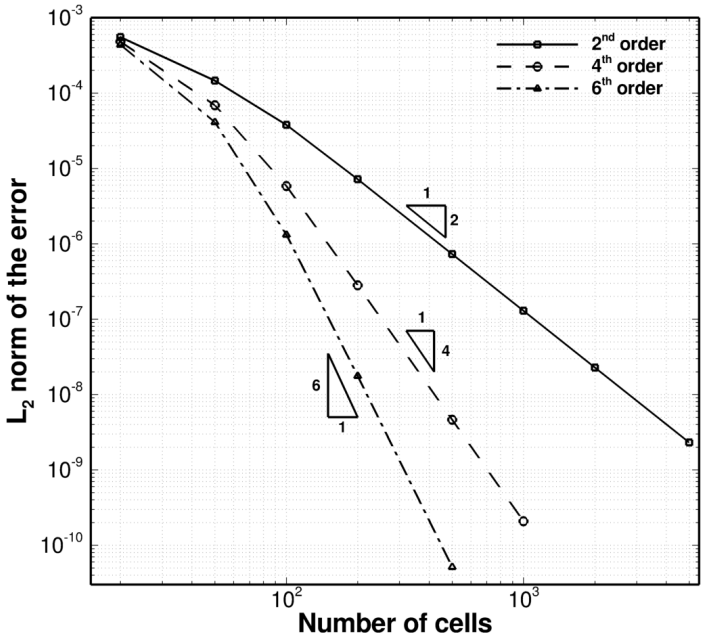

Figure 3.2: Error curves for 2^{nd}, 4^{th} and 6^{th} order central inviscid fluxes. Slope matches the theoretical value very well.

Due to symmetry only half the full problem is simulated and the $y = 0.5$ boundary has a symmetry boundary condition. The other three boundaries are adiabatic walls. The flow conditions and geometry are form Daru and Tenaud (2000). The solution is obtained using the sixth order inviscid fluxes and RK3 time integration on a grid with a resolution of 500×250. The Ducros switch is used for the numerical dissipation term.

At time $t = 0$ the membrane is 'removed' and the difference in the left and right states causes a shock to develop and begin traveling to the right, creating a boundary layer as it passes over the lower wall. When it reaches the end of the domain the shock reflects off the rightmost wall and begins traveling to the left, interacting with the boundary layer it has just created. This interaction can become quite complex with increasing Reynolds number. The solution is stopped at time $t = 1$ after a λ-shock and vortices are created in the wake of the shock.

Two Reynolds numbers are simulated: $Re = 200$ and $Re = 1000$. These are shown in Figure 3.3. Despite the strong shock in both cases there are no spurious oscillations. The lower Reynolds number has much less structure than the higher Reynolds number, as would be expected. Both solutions match the results of Daru and Tenaud (2000) as well as those of Yee and Sjögreen (2004), who performed their simulations with adaptive low-dissipative methods. These results are obtained on much coarser meshes.

3.3 Unsteady Horseshoe Vortex

The final problem is not actually a test problem, but the subject of study in Chapter 5. In that chapter the conditions and geometry are laid out in detail; in this case condition II is used ($p_o = 75$ psi). However, briefly, a Mach 6 boundary layer meets a cylindrical obstacle extruding from the wall of about the same height as the boundary layer. The cylinder causes a separation to form and several horseshoe vortices wrap around the leading edge of the roughness element. In addition, a bow shock forms off the leading edge of the cylinder which is extended into the supersonic freestream. The result is a somewhat complex shock/vortex structure that can become unsteady. In this case the horseshoe vortex system is unsteady (according to both experiment and simulations). As the system oscillates, it creates disturbances that travel downstream in the horseshoes and grow into helical shaped

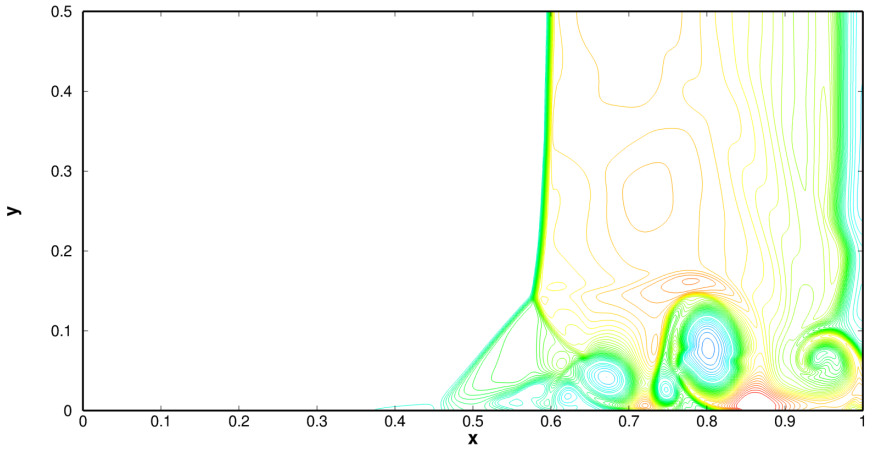

(a) Density contours for $Re = 200$

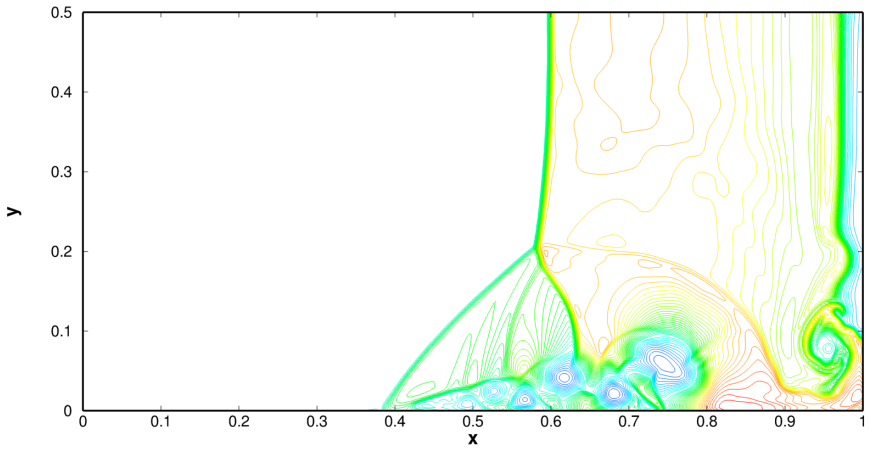

(b) Density contours for $Re = 1000$

Figure 3.3: Solutions for $Re = 200$ and $Re = 1000$ using sixth order fluxes. Results are in very good agreement with those of Yee and Sjögreen (2004) despite being on much coarser grids.

disturbances. These can be seen quite clearly using the 'Q' criterion (see Chapters 4 and 5) which can show locations in the flow where there are vortical structures.

These simulations are run using second order backward difference implicit time integration with a CFL of roughly two. The inflow boundary condition is prescribed from the result of a simulation of the full wind tunnel. The outflow is assumed supersonic and the walls are isothermal with a wall temperature of $T_w = 300$ K. The Ducros switch is used for the dissipation term.

The simulation is run with four flux schemes (Figure3.4): a third order upwind biased flux as well as the second, fourth and sixth order central flux. It is known from the experiment that the flow upstream of the roughness should be unsteady. However, with the third order upwind biased fluxes there is such a large amount of artificial viscosity that the unsteadiness is damped out and the flow becomes steady. By changing to the low-dissipation fluxes the flow becomes unsteady for all three orders of accuracy. Visibly, second order has only small perturbations in the instantaneous solution. Fourth order begins to show the structure of the helical disturbances and sixth order has very well defined helical structures.

Clearly the low-dissipation fluxes make this calculation possible as without it the prediction is steady flow, but this also makes evident the importance of the gradient reconstructed fluxes.

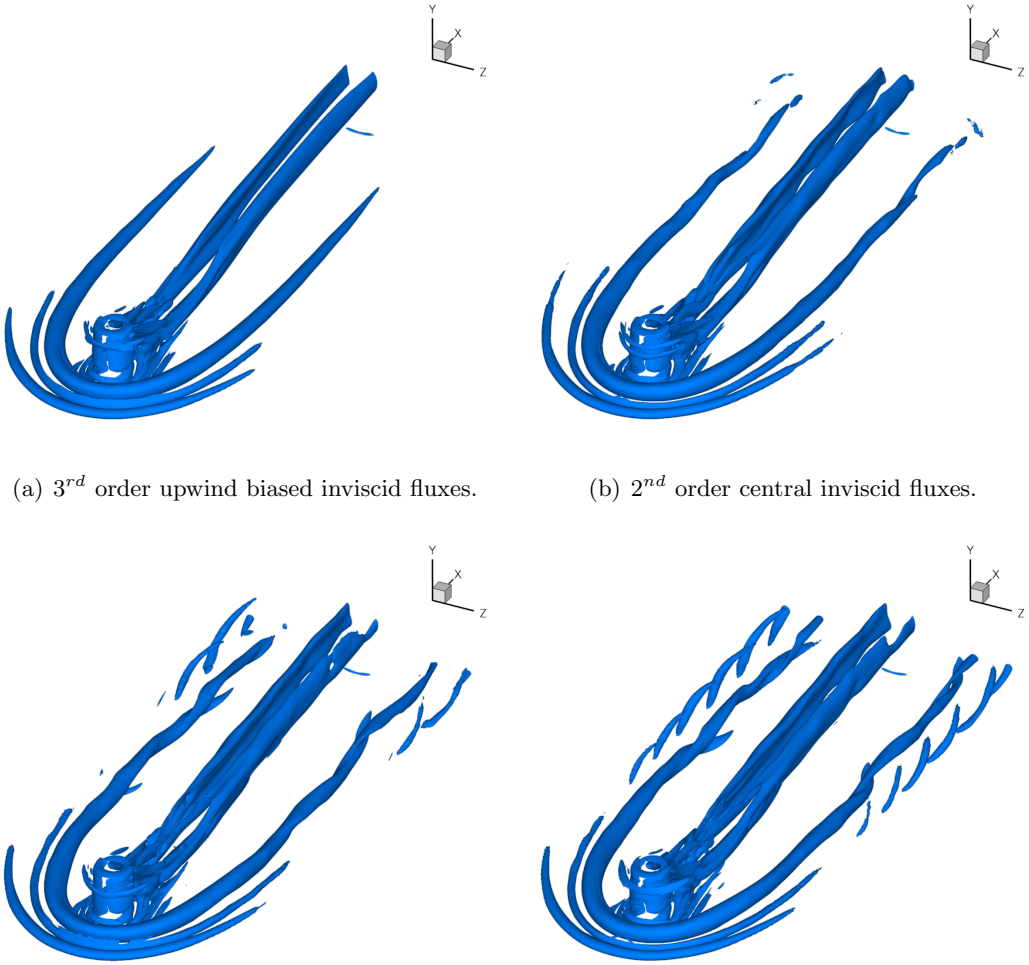

(a) 3^{rd} order upwind biased inviscid fluxes.

(b) 2^{nd} order central inviscid fluxes.

(c) 4^{th} order central inviscid fluxes.

(d) 6^{th} order central inviscid fluxes.

Figure 3.4: Q criterion iso-surfaces comparing several flux schemes. The importance of both the low-dissipation fluxes as well as the higher order fluxes can be seen by the presence of more structure.

Chapter 4

Natural Transition:
Flow Over an Elliptic Cone

The mechanism for transition in flight is often the growth of disturbances present in the freestream. The amplitude of the disturbances tends to be relatively small but as they enter the boundary layer they may grow and become large enough to cause transition. Several difficulties exist while trying to predict these transition phenomena.

Current approaches for predicting type of transition in hypersonic flows rely on correlations, such as Re_θ/M_e, or methods that predict the rate of disturbance growth in a boundary layer, such as linear stability theory (LST). Correlations (Re_θ/M_e) may be applied to specific geometries and flight conditions, but they do not represent the transition physics. As a result, the data does not collapse very well and the correct value of Re_θ/M_e to use is open to debate.

The parabolized stability equations (PSE) and the e^{N} semi-empirical method instead assume some disturbances in the freestream and track their growth as they convect in the boundary layer. This has shown to predict transition much better than the previous correlation, but still has some deficiencies. It can only predict the growth of a disturbance relative to its initial amplitude. This is what the N-factor is physically describing - the ratio of the disturbance's amplitude at a given location to its freestream value. Each experimental wind tunnel as well as conditions in flight must be calibrated. Nevertheless, this approach can reproduce experimentally measured transition locations for simple sphere-cone geometries, such as HIFiRE-1 (Alba (2008)). However, in complex flows it is not clear that a conventional boundary layer stability analysis approach will be valid. In this work a direct numerical simulation (DNS) is conducted on a flow undergoing transition due to

acoustic noise.

4.1 Introduction

Elliptic cones are of special interest due to the similarity between their geometry and many lifting bodies of hypersonic vehicles. These vehicle designs are often proprietary or classified which makes their study difficult. Even if a researcher had access to such a design, any analysis and results could not be disclosed to the academic community. For this reason it is useful to study a simple shape that also has a relatively similar geometry. Any conclusions or insights about the generic shape will most likely be relevant to other, similar, designs.

Elliptic cones have a relatively simple geometry, but still manage to create many interesting flow physics. An elliptic cone is simply a cone with an elliptic cross section, thus there is a major axis and minor axis ray of the cone. Often the major axis is referred to as the leading edge and the minor axis as the centerline or symmetry plane (though both are technically a plane of symmetry).

In supersonic flow, a conical shock forms around the cone. The shocks formed at the major axes are considerably stronger, due to a larger turning angle, generating greater regional pressure increases than shocks formed near the centerline. This creates a spanwise pressure gradient which 'pushes' flow toward the symmetry plane, i.e. develops crossflow. Low momentum fluid near the surface of the cone is overwhelmed by the pressure gradient and is turned away from the leading edge. Moving through the boundary layer in a path normal to the wall shows diminishing viscous effects becoming dominated by the flow inertia which turns the flow parallel to the rays of the cone and downstream. Further still from the surface and outside the boundary layer in the inviscid region, the flow is oriented along the rays of the cone (Figure 4.2). This profile exhibits an inviscid instability (Kimmel (1999)).

The opposing crossflows caused by the pressure gradients from the leading edges collide at the symmetry plane. This collision results in an accumulation of low momentum fluid which lifts the boundary layer as it becomes very thick relative to other locations on the surface. The boundary layer velocity gradient is shallow near the wall but becomes much steeper as the fluid accelerates to meet the post shock freestream. The change in velocity gradient creates a centerline boundary layer inflection point with an inviscid instability.

Figure 4.1 attempts to illustrate all of these features. There are now (at least) two different routes to transition: instability of the crossflow and instability of flow along the minor axis symmetry plane.

Experimental imaging of transitional boundary layers using filtered Rayleigh scattering (Huntley and Smits (2000)) was able to show much of the boundary layer structure during transition. Also, transition studies done by Holden et al. (2009) at CUBRC as well as studies done by Kimmel et al (1999) have made large strides in understanding the the behavior of the flow. Stability analysis (PSE) by Huang et al. (1995) on a 4:1 cone predicted that stationary crossflow vortices that develop in this region would be most unstable for some locations and could initiate transition at a Reynolds number as low as 1.3×10^5.

The HIFiRE-5 flight vehicle has a 2:1 elliptic cone as its nose cone. This slightly different geometry has very similar flow characteristics to a 4:1 elliptic cone. Berger et al. (2009) explored this geometry and found crossflow to be the primary cause of transition at zero angle of attack. In contrast to this, Kimmel et al (1999), also on a 2:1 cone, found that the inflected centerline boundary layer was the leading cause of transition. However, when artificial roughness was added the crossflow became the dominant instability. A 4:1 elliptic cone (relative to a 2:1 elliptic cone) has a larger spanwise pressure gradient and a larger surface area over which crossflow can develop. It may be reasonable to expect the crossflow to be the dominant instability in that situation. The work presented here is based on the 4:1 elliptic cone experiments done by Huntley and Smits at the Princeton Gasdynamics Laboratory.

4.2 Simulation Conditions

US3D was used to simulate these flows as described in Chapter 2. Fourth order inviscid fluxes and second order viscous fluxes along with second order backward difference implicit time integration were used. The Ducros switch is used for the added numerical dissipation in the inviscid fluxes.

Flow conditions correspond to four experimental conditions run by Huntley and Smits (2000) at the Princeton Gasdynamics Laboratory. According to the experimental results these conditions range from early transitional to fully turbulent. The tunnel has a freestream

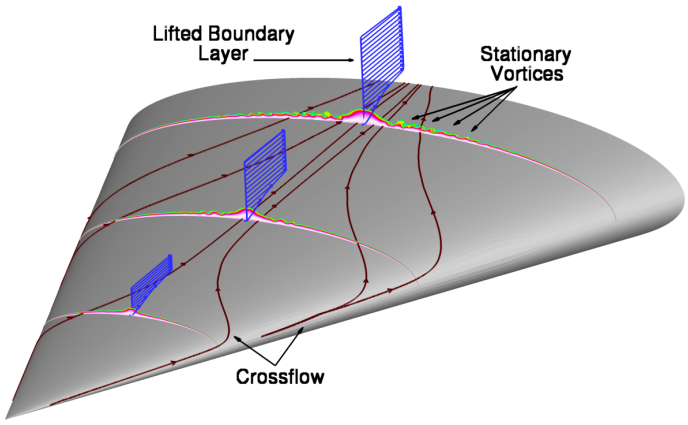

Figure 4.1: Crossflow on the surface causes streamwise vortices as well as a lifted boundary layer.

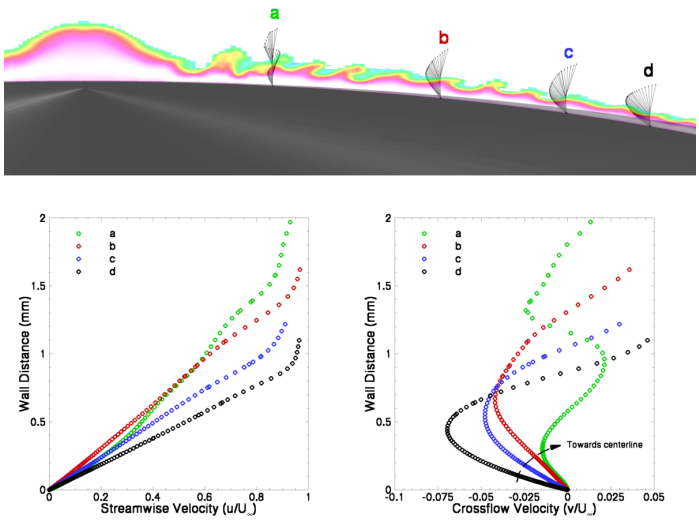

Figure 4.2: The top image has flow into the page and is going down the length of the cone. The contours show the vortices in the boundary layer as well as velocity vectors at a few locations. The lower plots show the skewed boundary layers that contain instabilities.

Mach number of 8 and a stagnation temperature of $T_o = 783$ K, giving test section velocity and temperature of $U_\infty = 1207.9$ m/s and $T_\infty = 56.7$ K. By changing the stagnation pressure, different Reynolds numbers are obtained and shown in Table 4.1. The length of the cone is 0.24 m and the major axis half angle is 17.5°. The nose radius of the elliptic cone model was measured to be less than 200 μm (Huntley (2000)). For simplicity in creating a computational grid the nose was assumed to be sharp.

Table 4.1: Simulation Conditions

Condition	Re [m^{-1}]	ρ [kg/m^3]	p_o [MPa]
1	5.4×10^6	1.666×10^{-2}	2.6
2	8.4×10^6	2.592×10^{-2}	4.1
3	11.3×10^6	3.487×10^{-2}	5.5
4	15.9×10^6	4.907×10^{-2}	7.8

The computations were done on half of the total geometry with a symmetry condition used on the major axis. This is a reasonable boundary condition considering the high pressure gradient leading away from this plane. The minor axis has unsteady flow which at times results in structure moving back and forth across the plane. It was found that putting a symmetry boundary condition there greatly stabilized the flow in an aphysical way. For this reason no boundary condition was used, rather the entire domain from major axis to major axis is computed. An isothermal wall boundary condition was used on the surface of the cone with a temperature of $T_w = 400$ K. This results in a relatively cold wall condition ($T_w/T_{aw} = 0.56$, assuming a recovery factor of $r = 0.9$). The inflow boundary condition is supersonic with the addition of acoustic noise described below. The grid was generated using the commercial packages GridPro and Gridgen and has approximately 35 million elements. Clustering near the wall ensures that the first point is within one wall unit to adequately resolve the boundary layer. In addition, a topology was used that allowed refinement in the streamwise direction while keeping an isotropic layer of hexahedral bricks in the crossflow and centerline area of interest (Figure 4.3). The 35 million element grid was partitioned to run on 256 processors.

The transition process selectively amplifies disturbances present in the flow. In flight, this is due to non-uniformity in the atmosphere. In wind tunnels, large Reynolds numbers cause the boundary layers on the walls of the wind tunnel to become turbulent. The

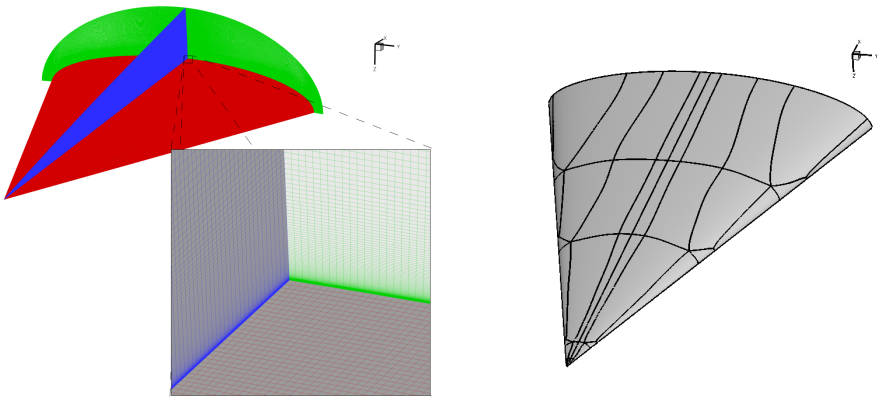

(a) Close up view of the grid showing the boundary layer region.

(b) Grid topology on the surface of the cone allows for refinement in the flow direction while keeping isotropic hexahedron elements near the centerline.

Figure 4.3: Grid construction is done carefully to ensure good results are obtained in the boundary layer region.

turbulent structures present in the boundary layer then radiate disturbances into the core of the flow in the form of acoustic waves. Since the simulations run in this study are based on experiments done at the Princeton University Gasdynamics Laboratory (Huntley (2000)), acoustic noise was added to the computational freestream to properly model the experiment. Noise spectra obtained from hotfilm measurements in the tunnel are used to construct numerical inflow disturbances with reasonably correct amplitudes. An assumption is made that these waves are essentially planar in the flow direction. In the strictest sense this isn't true, but it can be shown that for Mach 8 flow the maximum angle these waves can deviate from planar is about 7° and RMS mass flux fluctuations in the directions orthogonal to the flow direction are about 5% of the planar RMS mass flux fluctuation.

With this assumption, fluctuations are introduced in the freestream as a discrete approximation of the spectrum measured experimentally. Only an indirect measurement of the amplitudes of the spectrum were available in the form of voltage measurements from a hotfilm along with an RMS mass flux fluctuation, $(\rho u)'$, measurement of 2% of the freestream mass flux (Huntley (2000)). The method used to extract absolute amplitudes is as follows.

Pressure disturbances are introduced in the following form:

$$p' = \sum_k p'_k e^{i(\alpha_k^{\pm} x - \omega_k t)} \quad ; \quad \alpha^{\pm} = \frac{\omega}{U_o \pm a_o} \tag{4.1}$$

Where k is summing over the discrete spectrum being input, ω is the frequency of the disturbance and α depends on fast $(+)$ or slow $(-)$ moving waves. Using the solution to the linearized Euler equations for plane waves, fluctuations in the remaining flow variables are determined as:

$$\begin{pmatrix} \rho' \\ u' \\ T' \end{pmatrix} = \begin{pmatrix} \frac{1}{a_o^2} \\ -\frac{\alpha^{\pm}}{\rho_o(\alpha^{\pm} U_o - \omega)} \\ \frac{(\gamma-1)T_o}{\rho_o a_o^2} \end{pmatrix} p' \tag{4.2}$$

The magnitude of the fluctuations are set so that the integrated RMS mass flux fluctuations are 2% of the freestream mass flux, which is typical of tunnels of this type and consistent with the experimental measurements (Figure 4.4).

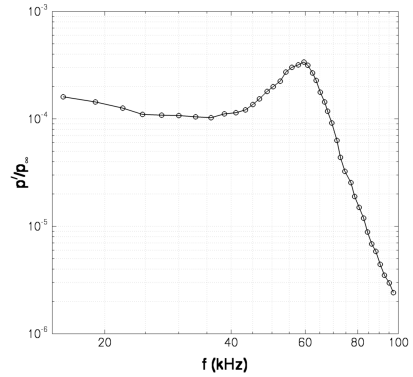

Figure 4.4: Spectra of pressure fluctuations added to inflow.

4.3 Results

A solution without acoustic noise is computed first and allowed to converge as far as possible. In the higher Reynolds number cases the solution never 'converges' due to unsteadiness. Starting from this solution, acoustic noise is added to the freestream and the simulation continued with a constant time step of 5×10^{-9} seconds. This corresponds to a global CFL of roughly 10^3 due to the extremely small grid cells near the sharp nose of the cone; however,

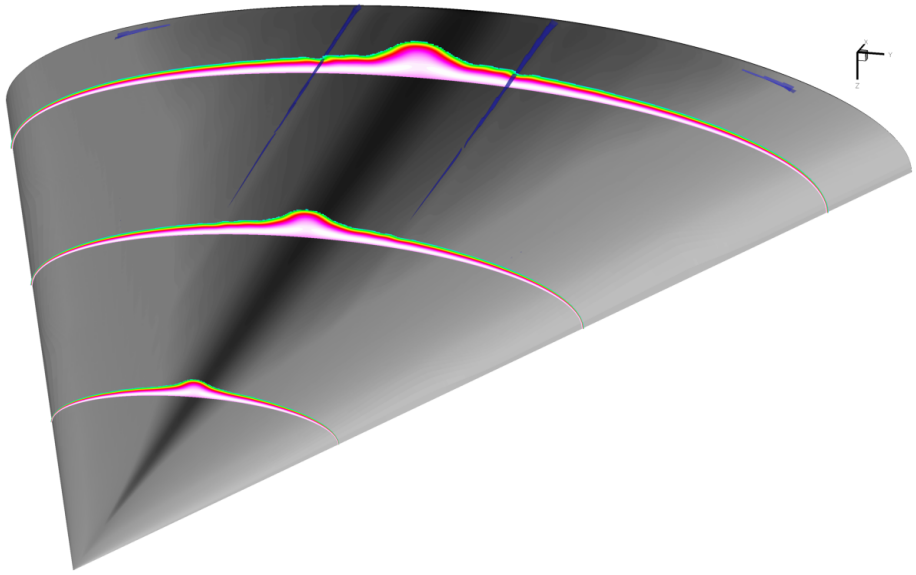

Figure 4.5: Mean flow field for Re $= 5.4 \times 10^6$ m^{-1}. Surface shaded according to mean heat flux. Planes of temperature contours taken at 7, 14, and 21 cm from the tip of the cone. Blue iso-surfaces are of Q [Defined in paper].

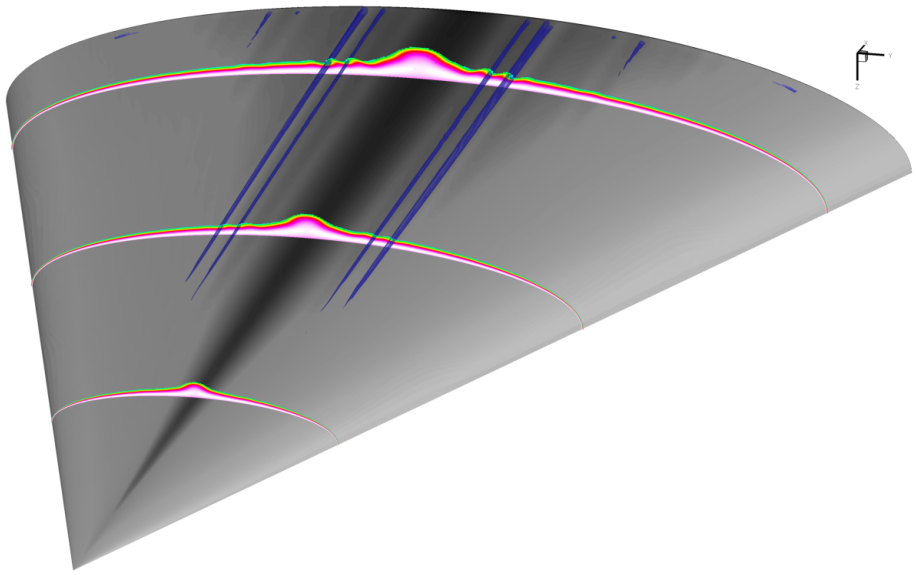

Figure 4.6: Mean flow field for Re $= 8.4 \times 10^6$ m^{-1}. Surface shaded according to mean heat flux. Planes of temperature contours taken at 7, 14, and 21 cm from the tip of the cone. Blue iso-surfaces are of Q [Defined in paper].

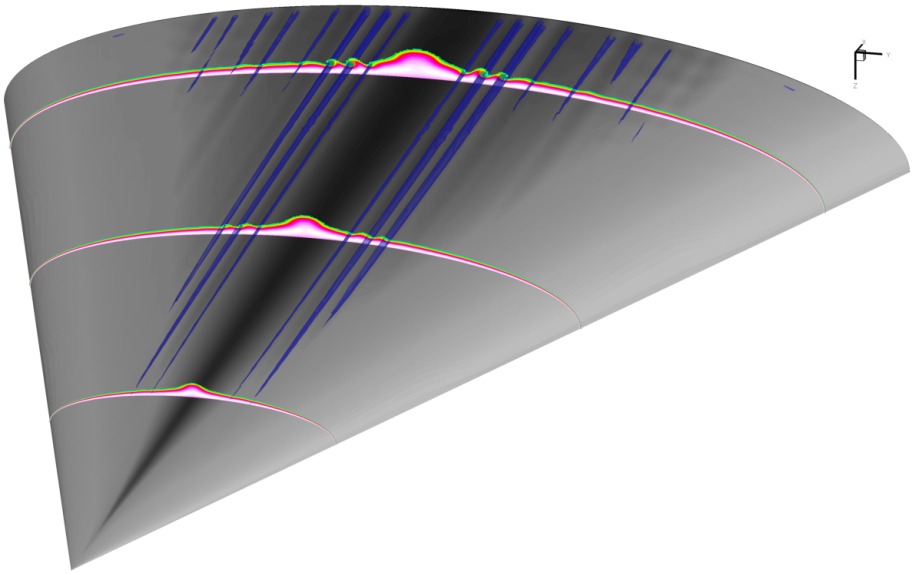

Figure 4.7: Mean flow field for Re = 11.3×10^6 m^{-1}. Surface shaded according to mean heat flux. Planes of temperature contours taken at 7, 14, and 21 cm from the tip of the cone. Blue iso-surfaces are of Q [Defined in paper].

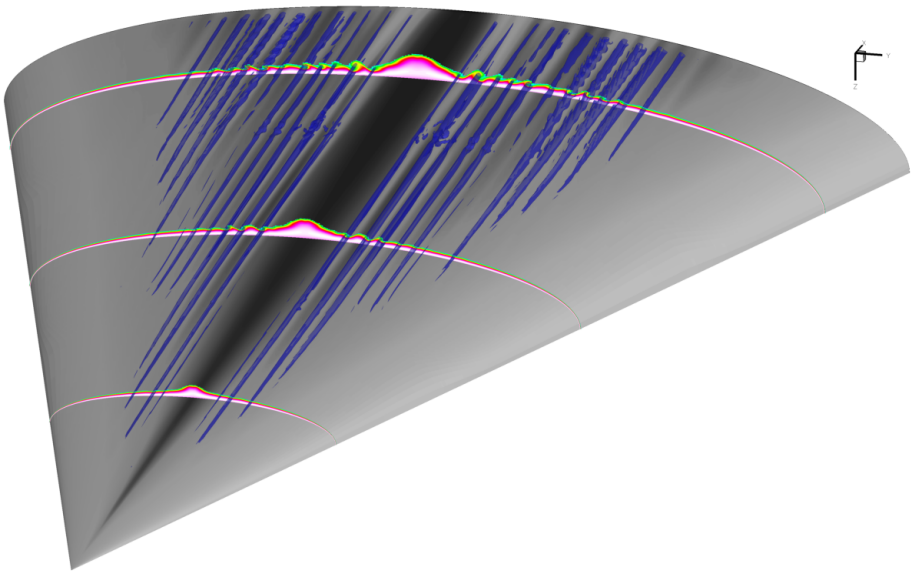

Figure 4.8: Mean flow field for Re = 15.9×10^6 m^{-1}. Surface shaded according to mean heat flux. Planes of temperature contours taken at 7, 14, and 21 cm from the tip of the cone. Blue iso-surfaces are of Q [Defined in paper].

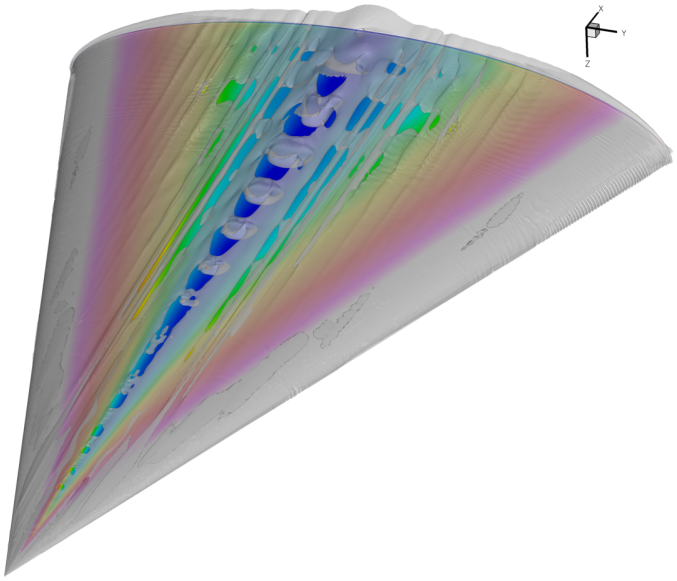

Figure 4.9: Instantaneous flow field for Re $= 5.4 \times 10^6$ m^{-1}. Surface contours are instantaneous heat flux. Iso-surfaces are of Q.

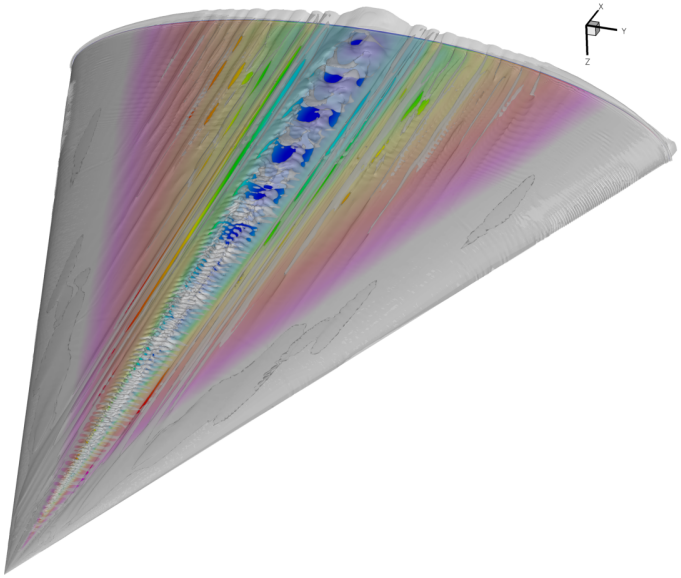

Figure 4.10: Instantaneous flow field for Re $= 8.4 \times 10^6$ m^{-1}. Surface contours are instantaneous heat flux. Iso-surfaces are of Q.

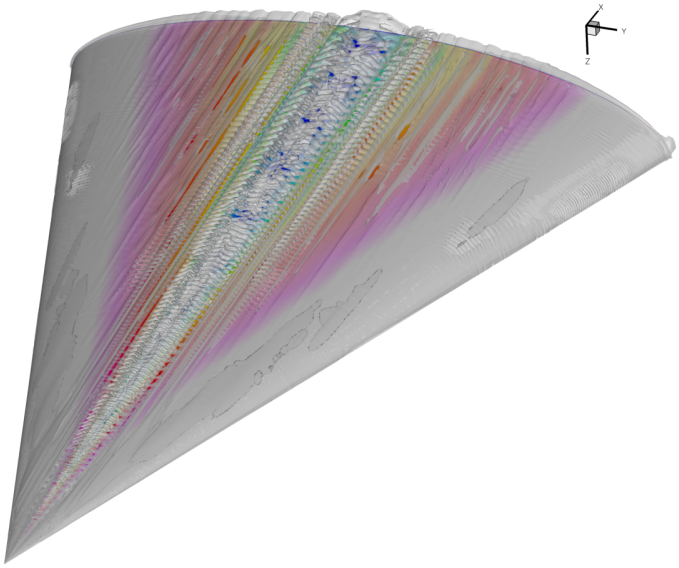

Figure 4.11: Instantaneous flow field for Re $= 11.3 \times 10^6$ m^{-1}. Surface contours are instantaneous heat flux. Iso-surfaces are of Q.

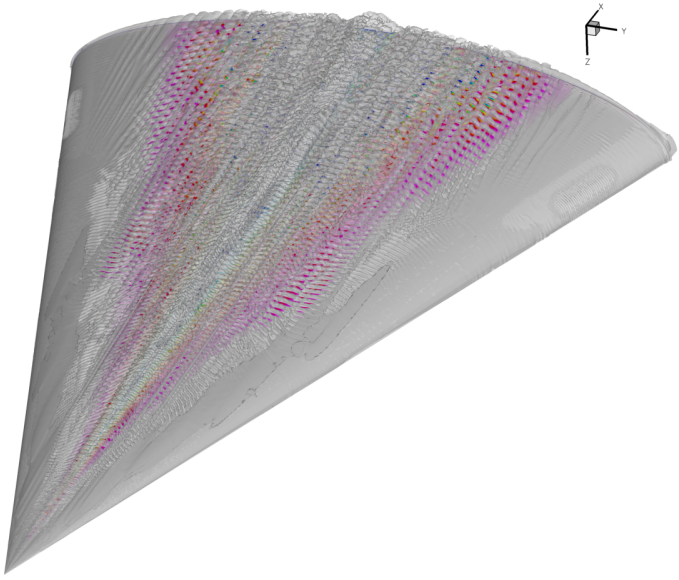

Figure 4.12: Instantaneous flow field for Re $= 15.9 \times 10^6$ m^{-1}. Surface contours are instantaneous heat flux. Iso-surfaces are of Q.

the time step was chosen such that away from the nose of the cone the local CFL is less than unity. This ensures that the numerical dissipation associated with the implicit method is reduced as much as possible and also that the time step is small enough to resolve the time scales in the flow. Utilizing 256 processors, this time step takes about five days of runtime to simulate one flow through time, defined by the cone length and freestream velocity. Several flow through times are required to allow the acoustic noise to permeate the entire domain.

A useful parameter used to visualize the structures that form in the flow is the Q criterion, or the second invariant of the velocity gradient tensor which essentially indicates regions of the flow which are 'swirling'. Iso-surfaces of Q are able to visualize both the crossflow vortices as well as structures along the centerline. Figures 4.5 - 4.8 show Q for the mean flow of the four conditions simulated. The crossflow vortices can be seen starting at a point a distance from the leading edge and then continuing down the length of the cone. With contours of temperature plotted at three locations in the streamwise direction the crossflow vortices clearly intersect the structures in those planes. Also, the number of crossflow vortices increases with Reynolds number as well as the strength of the vortices.

Naturally, the instantaneous flow fields contain much more activity than the mean flow field. Iso-surfaces of Q show the rollup of the crossflow vortices in the streamwise direction as well as the larger structures on the centerline. These flow features are displayed in Figures 4.9 - 4.12 and discussed below.

The structure of the mean flow changes over a relatively small range of Reynolds number. This is very evident by looking at a spanwise plane 21 cm from the tip of the cone (Figure 4.13). Contours of temperature show the lifted boundary layer along the centerline as well as the crossflow vortices. The waves in the crossflow direction resemble classic Kelvin-Helmholtz instability waves. As the Reynolds number increases, the number of crossflow vortices also increases. Crossflow boundary layer profiles show the boundary layer thickness decreases which causes gradients in the boundary layer to increase as can be inferred from Figure 4.14.

The structures that form from the crossflow are stationary and form at certain locations. This discreteness seems to be caused by some critical boundary layer inflection, but also from interactions between neighboring vortices and from the vortex closest to the centerline interacting with the centerline bulge. The first crossflow vortex forms next to the centerline

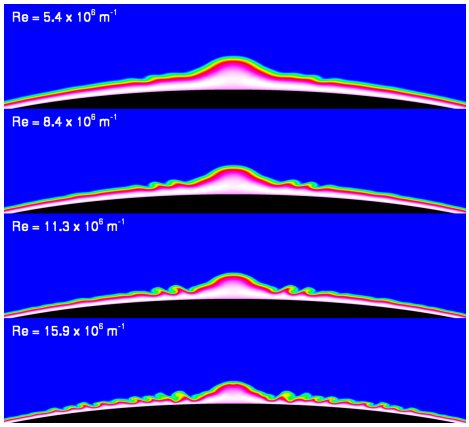

Figure 4.13: Mean temperature contours in a spanwise plane 21 cm from the nose of the cone for Reynolds numbers ranging from 5.4×10^6 to 15.9×10^6 per meter

bulge, while the second crossflow vortex forms next to the first vortex and so on. These can be easily seen by plotting the heat flux across the span of the cone. As the vortices alternately lift and compress the boundary layer the heat flux will fall or rise, respectively. Figure 4.15 shows heat flux across the span of the cone 21 cm from the nose. Condition 1 has few crossflow vortices present near the centerline while conditions 2 and 3 show a slight increase in the number and intensity of these crossflow vortices, with more becoming present further from the centerline. However, condition 4 suddenly has evidence of many more crossflow vortices, indicating that somewhere between these Reynolds numbers an interaction takes place.

Crossflow vortices can be seen in the mean flow heat flux spanning the cone, but looking at instantaneous heat flux contours on the surface presents an explanation for the sudden deviation from the trend the vortices had been following for the three lower Reynolds numbers. At the highest Reynolds number, the flow is unsteady even without freestream forcing, but doesn't transition or deviate much from the mean flow, while the lower Reynolds numbers are steady without acoustic noise. When freestream acoustic noise is added to the inflow, it travels into the domain and boundary layer and waves begin to form in the streamwise direction on top of the stationary vortices (Figure 4.16).

Because of the inflected boundary layer in the crossflow, there is reason to believe it will be susceptible to instability. At lower Reynolds number these crossflow vortices appear to remain stable with the addition of disturbances at the specified wavenumbers. With an

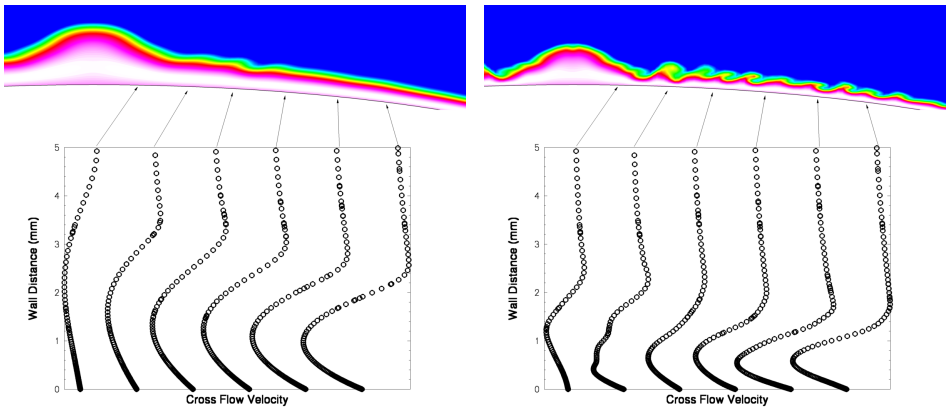

(a) Condition 1 (b) Condition 4

Figure 4.14: Temperature contours of a spanwise plane 21 cm from cone tip. Crossflow velocity vectors 0.5, 1.0, 1.5, 2.0, 2.5, and 3.0 cm from the centerline.

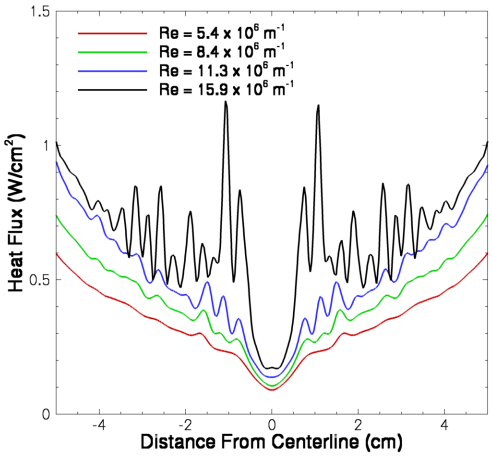

Figure 4.15: Heat flux spanning the cone 21 cm from the nose of the cone.

Figure 4.16: Contours of density in the boundary layer. Flow is from left to right in a plane about 1 cm from the centerline. This location corresponds to the first vortex next to the centerline.

increase in the Reynolds number the vortices begin to respond to the disturbances and begin to rollup in the streamwise direction. This rollup appears to create secondary disturbances as the faster moving fluid above the boundary layer moves over the waves. Additionally, the vortex closest to the centerline seems to shed these disturbances into the bulge of the centerline boundary layer.

Along the symmetry plane the lifted boundary layer becomes quite thick with a clear inflection point. Figure 4.17 shows both the growth of the boundary layer as well as its inflection point. This causes the centerline to have its own instabilities and wave growth is observed of a much larger wavelength than the disturbances in the thinner, off centerline boundary layers. These can be seen most clearly for condition 1 where the rest of the flow is relatively quiet (Figure 4.18). Large waves a few boundary layer thicknesses in length form and travel down the symmetry plane. Left to themselves these waves would continue to grow and eventually transition if the cone were long enough.

At the larger Reynolds number the breakdown of vortices near the bulge appears to cause a secondary transition mechanism. The rollup in the streamwise direction of the vortex creates waves which in turn cause disturbances. These secondary disturbances get shed in the thick centerline boundary layer. Inside the boundary layer, the waves reflect and bounce back and forth and coalesce. This seems to contribute to the centerline being more unstable.

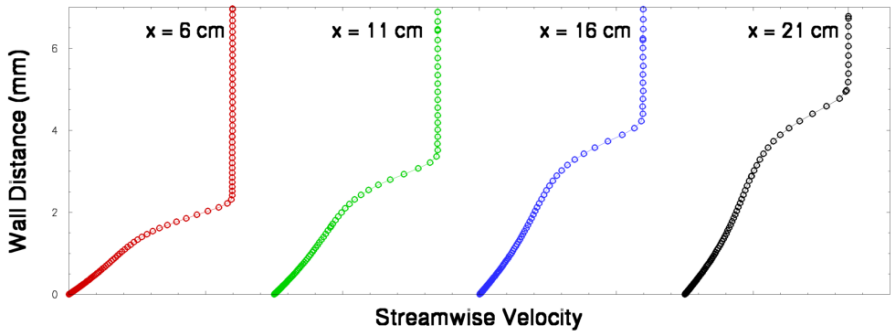

Figure 4.17: Velocity profiles at four locations down the center of the minor axis of the cone.

Disturbances from the crossflow that travel downstream inside the centerline boundary layer are emanated oriented in the flow direction. Continuing downstream and traveling

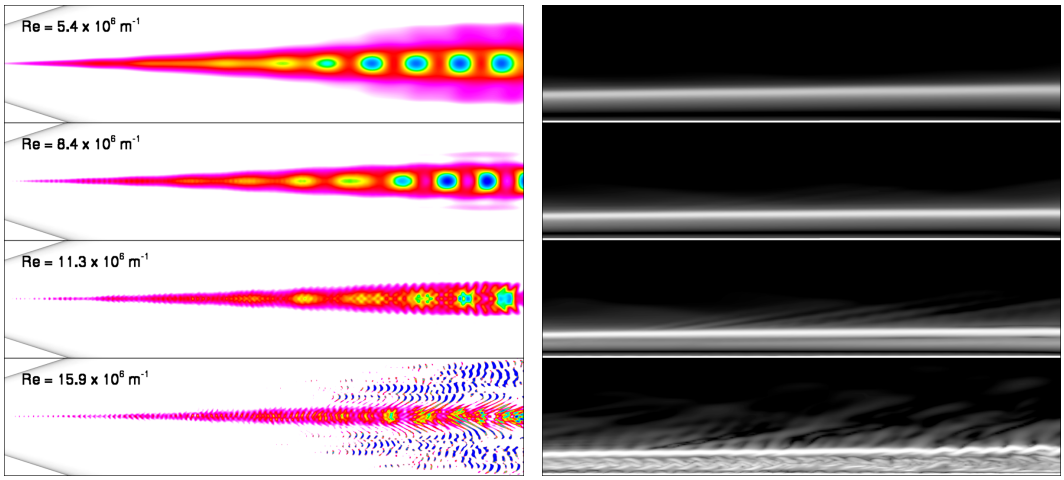

(a) Heat Flux Contours (b) Density Gradient Magnitude Contours

Figure 4.18: On the left are heat flux contours from a planform view of the cone. Clearly visible are the large scale structures as well as the breakdown of the crossflow. On the right are density gradient magnitude contours of the boundary layer in the crossflow vortex 1 cm off from the centerline. Flow is left to right.

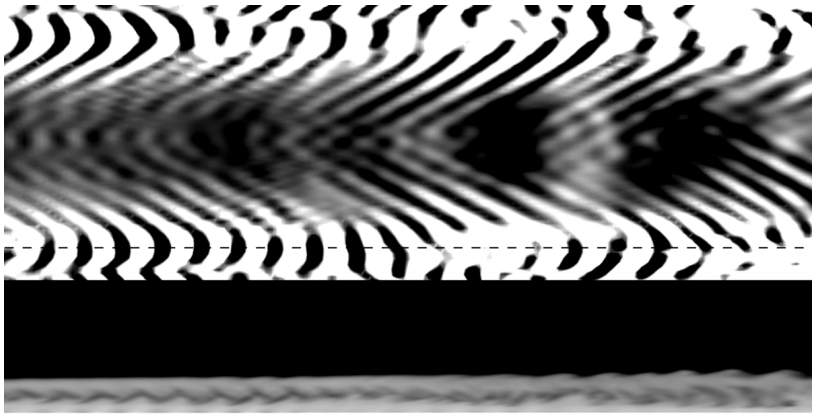

Figure 4.19: The upper image is heat flux contours on the centerline. The lower image is density contours in the boundary layer through the dashed line in the upper image. Both images are for condition 4. Flow is left to right. The center of the image is 21 cm from the front of the cone and the frame size from left to right is 6 cm.

at the local flow conditions, the disturbances begin to reflect back and forth within the boundary layer. While oriented downstream they remain separated from each other and don't interact, but as the angle gets steeper and they bounce back and forth many more interactions occur. For condition 3, the second highest Reynolds number, the angle of the disturbances shed from the vortex appears to be roughly 45° by the end of the cone and this angle becomes steeper for condition 4. This is happening in concert with the much larger waves from the centerline instability moving in the streamwise direction. When a coalescence of the secondary disturbances meets with a centerline wave a large increase in pressure and heat flux is observed that looks similar to a turbulent spot (Figure 4.19). Whether or not this is in fact a turbulent spot is uncertain at this point, but it appears these simulations are capturing nonlinear disturbance growth.

Chapter 5

Roughness Induced Transition: Flow Over A Cylindrical Roughness Element

Natural transition was explored in the last chapter by introducing acoustic noise into the domain. One difficulty, as described previously, with this approach is the lack of information about the form the noise takes, both in wind tunnel facilities as well as in the atmosphere. It is known that there are fluctuations in the freestream, but quantifying these fluctuations has not been done to much accuracy. Often just a mass flux fluctuation is quoted from hotwire measurements. But frequency content, as well as disturbance amplitude as a function of frequency, is needed. Also, to be completely accurate, the planar wave assumption should be discarded as well.

Not all transition is caused by freestream disturbances growing and eventually becoming large enough to trip the boundary layer. Real flight vehicles have surface imperfections which can also create disturbances or alter the flow and make it more susceptible to transition. In this chapter the focus is turned toward situations where transition is driven by surface roughness.

5.1 Introduction

As has been described in the last chapter, boundary layer transition drastically alters skin friction and heating rates, making accurate predictions crucial to hypersonic vehicles and their design. Transition of boundary layers comes about due to disturbances in the flow that find 'favorable' conditions and amplify. Flow disturbances, in some cases, are present in the free-stream (typically of small amplitude), but roughness can also cause transition to

occur before the natural location. In some situations it is beneficial for the boundary layer to become turbulent, such as preventing scramjet engines from unstarting, and tripping the flow with roughness elements may be desirable. Incorrectly assuming a transitioned boundary layer can be just as disastrous as incorrectly assuming a laminar boundary layer on a vehicle's exterior. The roughness may be distributed over the surface in the form of many small imperfections (distributed roughness) or may exist as a single, isolated, protuberance. In this chapter, the focus is on studies of flow over a surface with an isolated roughness element.

Prediction of transition in such flows is typically done using correlations based on parameters such as the roughness-height Reynolds number, Re_k. These correlations are often made in ground-based facilities and then extrapolated to flight cases. Better methods that incorporate the physics of the flow are needed, but details of the flow field are required for this to be realized. The physics of roughness-induced transition are poorly understood, and experimental measurements of roughness-induced instabilities at supersonic and hypersonic speeds are limited. An isolated roughness often generates a wake with streamwise vortices originating from within the separation region upstream of the roughness. Streaks from vortices were observed in oil-flow visualization by Whitehead in 1969. Flow structures oriented in the streamwise direction have also been observed in recent high-speed experiments (Danehy (2010)). For large roughnesses ($k/\delta \approx 1.0$ or greater), the dominant instability type is likely to be an "absolute" instability. Absolute instabilities grow in time from an initial disturbance and are oscillatory in nature (Huerre (1990)). Examples of absolute instabilities include periodic vortex shedding, as observed in low-speed roughness experiments (Acarlar (1987)), or some other instability caused by the large disturbance of the flow by the roughness. For smaller roughnesses (as the roughness height tends towards zero), it is likely that "convective" instabilities within the shear layers generated by the roughness become the dominant mode of transition. Convective instabilities are characterized by spatial growth as they are swept downstream and are subject to the effects of external disturbances. Other possible transition mechanisms include that of transient growth (Reshotko (2004)), interaction of streamwise vorticity from the roughness with the Görtler instability or stationary crossflow (Schneider (2008)), or modification of the receptivity of the boundary layer. Direct numerical simulations (DNS), such as those presented in this paper, allow

for detailed analysis of the flow field and can provide the insight needed to quantify the roughness-induced transition process.

The experiments being simulated here were done in the Mach 6 quiet wind tunnel at Purdue University (Wheaton (2009). A cylindrical roughness element is extended into a laminar boundary layer to create disturbances that may cause the boundary layer to transition (Figure 5.1). Simulations of this experiment have been performed before (Greene (2009)); however, approximations that were made to the geometry in that work are not made here and so more accurate results are obtained. Simulations of similar experiments (Chang et al.(2010) and Choudhari et al. (2010)) have been done as well, but a quantitative comparison of the frequency of the instability (between experiment and computational fluid dynamics (CFD)) has not been presented.

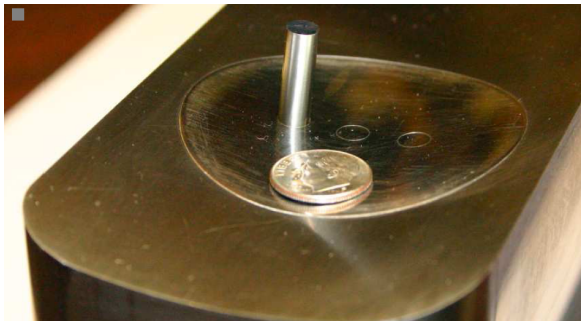

Figure 5.1: Photograph of the roughness element (which is actually a micrometer head) in the wind tunnel wall (Wheaton (2009)).

In the work presented here, the complex flow structures created by the roughness element are explored for several flow conditions along with the state of the boundary layer downstream of the roughness. Note that while the effect of freestream disturbance on flows of this sort is expected to be significant, it is not considered in this paper – transition and breakdown to turbulence occurs (for the higher Reynolds number cases) solely due to the presence of the roughness element.

The chapter is organized as follows: first, a description of the experiment is given as well as a brief section on the simulation setup. Second, several flow conditions are simulated for a constant roughness height that range from laminar to transitional to turbulent. Then, for constant flow conditions, the effect of changing the roughness height is explored. Finally, some conclusions are presented.

5.2 Description Of The Experiment

Experimental measurements of roughness-induced instabilities were obtained in the Boeing/AFOSR Mach-6 Quiet Tunnel (BAM6QT) at Purdue University and are the first known measurements of this kind at hypersonic speeds (Wheaton (2009) and Ward (2010)). The Boeing/AFOSR Mach 6 Quiet Tunnel at Purdue University is a low-noise hypersonic facility used in boundary layer transition research. While most hypersonic wind tunnel walls have turbulent boundary layers, the BAM6QT employs a bleed slot upstream of the throat to remove the existing boundary layer. This keeps the boundary layer laminar along the tunnel walls which is extremely useful in low noise transition research, but in this work it is the thick laminar boundary layer that is also of interest. The laminar boundary layers produced can be as thick as 20 mm (Wheaton (2009)); however, in the conditions presented here the boundary layer thickness is on the order of 10 mm.

An insert for the wind tunnel wall was designed to allow for a Starrett model 263L-38TN micrometer head (that functions as the isolated roughness element) to be extended into the flow. The micrometer head is cylindrical with a diameter (D) of 5.97 mm and can be extended up to a height (k) of 24.31 mm (accurate to 0.05 mm). The location of the roughness element is 1.924 meters downstream, which from this point on will be referred to as x_o and x locations will be in reference to this location (e.g. $x = 1D$ is one diameter downstream of x_o) of the nozzle throat. Measurements in the wake are taken by a pitot probe and a hotwire on the centerline as well as at locations two diameters off the centerline.

The hotwire probes were built at Purdue University specifically for operation in the thick boundary layer of the tunnel wall. A Kulite XCQ-062-15A piezoelectric pressure transducer is housed inside the pitot probe and is used to make dynamic measurements of disturbances in the boundary layer. The frequency response of the pitot probe is lower than the hotwire, but both are expected to be able to resolve the frequencies that are estimated to be present. For a detailed explanation of the probes, as well as a discussion of their experimental advantages and disadvantages, see Wheaton et al. (2009, 2010).

5.3 Simulation Conditions

US3D was used to simulate these flows as described in Chapter 2. Sixth order inviscid fluxes

and second order viscous fluxes along with second order Crank-Nicolson point implicit time integration was used. The Ren switch using density was employed for the added numerical dissipation in the inviscid fluxes.

An isothermal wall assumption is used with a wall temperature of 300 K. This is strictly speaking not accurate as the temperature is 433 K (T_o) at the nozzle throat and then drops towards room temperature downstream. An analysis done at Purdue found that the temperature quickly drops after the throat and from there asymptotes to room temperature. From this analysis it was decided that an isothermal wall at room temperature was an adequate representation of the wall temperature.

A supersonic outflow is used despite the thick boundary layer. This is because the boundary layer is subsonic only very near the wall and it was found that the placement of the outflow had no effect upstream.

Simulating the entire tunnel from the nozzle throat is not feasible as the range of length scales would make the grid size prohibitively large. Therefore, the simulation is done in two pieces. The first is an axisymmetric simulation of the entire wind tunnel from upstream of the nozzle (without the roughness element). The second uses the axisymmetric results as an inflow in the full grid. For the first part a 'pie' grid (wedge shaped cells running the length of the domain) was used (size $2000 \times 1200 \times 2$) to adequately resolve the boundary layer. The three conditions of interest have stagnation pressures of $p_o = 60, 75$ and 90 psi (413, 517 and 620 kPa, respectively). A characteristic subsonic boundary condition was used with these conditions as the inflow and the boundary layer profile at x_o extracted as the inflow for the full grid. Mach contours for the full tunnel solution at condition III is shown in Figure 5.2. The extracted boundary layer compares very well to the experimentally measured boundary layers, giving confidence in its accuracy and using it as the inflow in the full simulation (Figure 5.3).

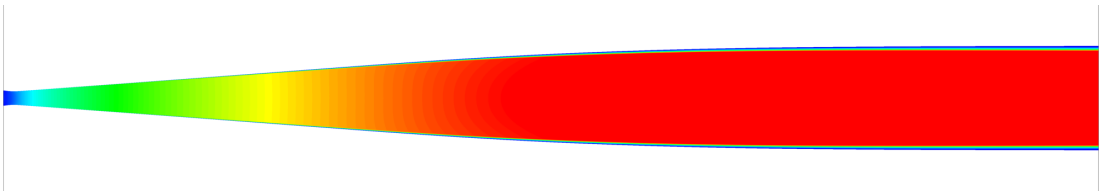

Figure 5.2: Mach contours for the BAM6QT.

Construction of the three dimensional grid for the roughness element calculations was done with the commercial package GridPro. GridPro makes multi-block grids, which, though technically structured, allow for essentially unstructured grids. For example the large grids used in this chapter have over 50,000 blocks, making it impossible (for all practical purposes) to use with a structured code. This ability also allows for doing 'nested-refinement'. This was done to a much lesser extent in the last chapter to allow the grid to maintain grid spacing along the length of the cone. In this case the grid has a high-resolution 'corridor' around the roughness element and its wake that can resolve the structures created by the presence of the cylinder. Away from this corridor, the grid is derefined quickly in order to keep the total grid size manageable. Figure 5.4 shows a part of the grid near the roughness element.

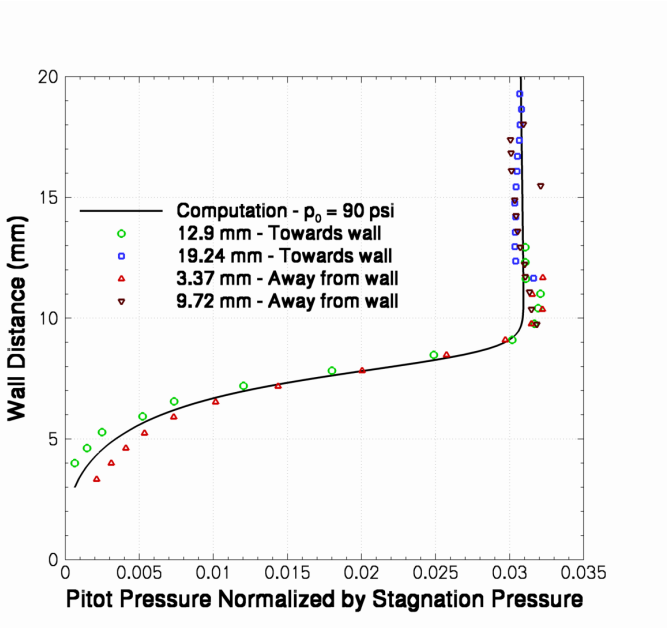

Figure 5.3: Boundary layer profile for condition III. Symbols are data from the experiment.

Two domain sizes are used for these simulations. The smaller grids extend 25 roughness diameters ($25D$) upstream and $10D$ downstream of the center of the roughness element. The larger grids extend $75D$ downstream. The full wind tunnel cross-section is included to simplify boundary conditions. In the high resolution 'corridor' around the roughness element the grid has a variable resolution which is explored in a later section. Grid sizes for the smaller domain range from 5-70 million elements. The large domain, which extends

further downstream, has a resolution of 32 points per diameter. This results in a grid of 270 million elements. The first grid point off the wall is at a constant distance of 0.1μm which is within one wall unit to resolve the boundary layer.

A time step $\Delta t = 5 \times 10^{-8}$ seconds is used which corresponds to a CFL number near three close to the wall and less than one away from the wall. This ensures that the relevant time scales are resolved.

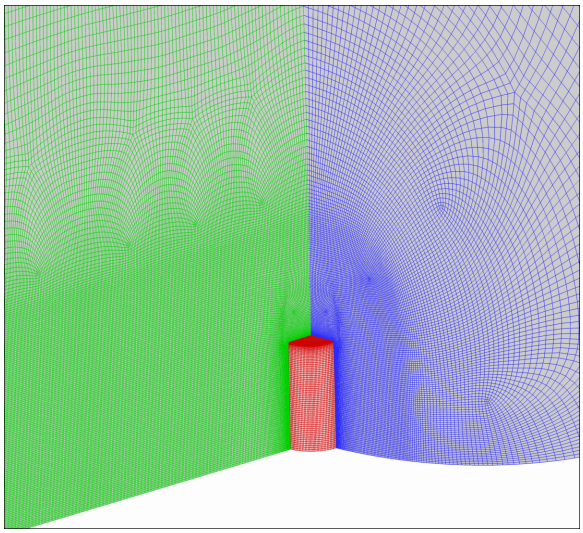

Figure 5.4: The grid close to the roughness element is very dense, but is derefined away from it in order to keep the total grid size manageable.

5.4 Results

5.4.1 Constant Roughness Height : $k = 10.2$ mm

The first section will focus on a constant roughness height with varying freestream conditions. The height, k, was chosen to be 10.2 mm to correspond to the work done by Wheaton at Purdue. They had chosen that height due to interest in 'large' roughness elements in which the ratio of roughness height to boundary layer thickness was roughly one or greater. Three different conditions were chosen which the data seemed to indicate would span from laminar to transitional to turbulent. These conditions, corresponding to tunnel stagnation pressures of 60, 75 and 90 psi (the tunnel stagnation temperature is held constant at 433 K), are computed. These conditions are referred to as condition I, II, and III, respectively (not

to be confused with conditions 1,2,3 and 4 from the previous chapter). Solutions are first obtained on the full tunnel geometry using the axisymmetric grid and the resulting profiles are used as inflow conditions for the full scale simulations. Pitot pressure measurements in the boundary layer are available at condition III – comparison of the numerical result with this data is very good (Figure 5.3) and gives a measure of confidence in the accuracy of the inflow data. The centerline Mach number and centerline static temperature are 6 and 53 K, respectively. The different stagnation pressures, as expected, produce different boundary layer thicknesses at the roughness element location; the various parameters are summarized in Table 5.1 below. These correspond to boundary layers at the roughness location when the roughness is not present.

Table 5.1: Simulation Parameters

Condition	$p_\circ$ [psi]	δ [mm]	k/δ	Re_k
I	60	10.4	0.98	4.8×10^4
II	75	9.1	1.12	5.9×10^4
III	90	8.3	1.23	7.0×10^4

Description of the flow:

There are several important features that develop in a flow of this kind. The dominant flow feature is a system of horseshoe vortices that form in the upstream separation and wrap around the cylinder. Following the convention of Baker (1979), who studied the laminar horseshoe vortex in detail, the present flow contains a six vortex system. The six vortices are three pairs of counter-rotating vortices with the 'primary' horseshoe vortex – the largest and closest to the cylinder – being particularly active in determining the state of the downstream flow. In past low speed experiments the horseshoe vortex system has been beautifully visualized in experiments by E.P. Sutton (printed in Thwaites (1960) and shown in Figure 5.5).

In the current work the flow is supersonic – Mach 6 at the boundary layer edge – and this creates shock structures in the upstream separation region. An oblique shock forms and passes through the primary vortex before joining the bow shock that forms in front of the roughness element. Behind this bow shock the pressure rises significantly and flow travels away from this point in all directions, including towards the wind tunnel wall. When looked

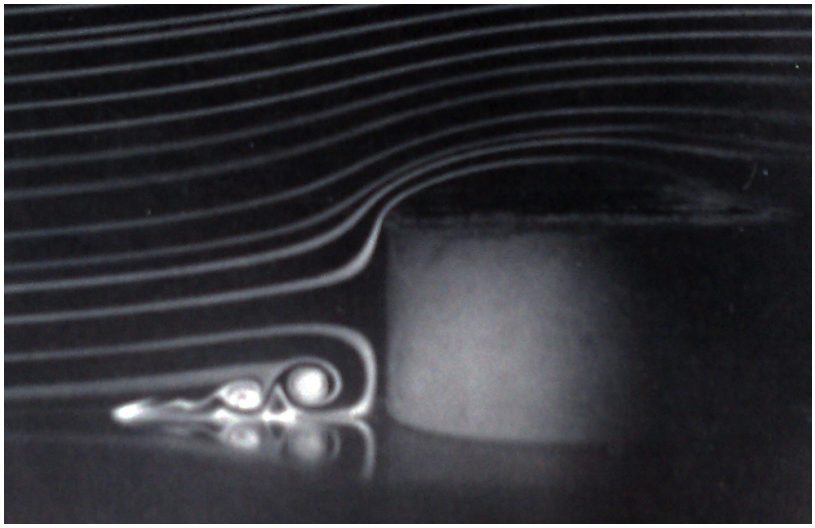

Figure 5.5: Low speed flow visualization experiments by E.P. Sutton (printed in Thwaites (1960)) shows the horseshoe vortex upstream of a roughness element.

at on the symmetry plane, behind the bow shock is a jet from the upper area of the cylinder down towards the wall-cylinder junction where the flow then has to turn upstream and feed back into the primary vortex. The interaction of the primary vortex, the shocks and the 'jet' can be steady or unsteady, depending on the Reynolds number. It's found that the lowest Reynolds number (condition I) is steady while the other Reynolds numbers (conditions II and III) become unsteady. Condition II is slightly unsteady, going through the following cycle: The jet pushes fluid into the primary vortex which then swells. As it swells, the bow shock moves away from the cylinder and the pressure drops. This causes the jet to lose strength and push less fluid into the primary vortex which shrinks in size, allowing the shock to move closer to the cylinder. As the pressure goes up, the jet increases in strength and the process repeats. Condition III goes through this process as well, though the size of the oscillations is much larger. Also, the jet is much stronger on average for condition III and it separates from the cylinder as it travels down toward the wall junction. Three additional vortices form in this region which also contribute to the unsteadiness. This is very similar in nature to the spike-tip instability (Maull (1960) and Fesztl (2004)). Although the geometry is different, in spike-tip flows the process is described with an inflationary stage and collapsing stage that are extremely similar to the current flow.

This unstable interaction that occurs in the upstream separation region is a very important aspect of the flow. It creates disturbances that get sent downstream and can cause transition. A comparison between the experimentally measured disturbance frequency and a numerical simulation has never been done before this work. Part of the difficulty is in the sensitivity of the upstream unsteadiness to artificial viscosity. An upwinded method is likely to damp out all unsteadiness as shown in Chapter 3; even if disturbances are created, they will be damped out downstream before they can grow and cause transition. The low dissipation and high order accuracy is vital to the computation of this flow.

Downstream from the roughness are two important catalysts for transition. The first is the result of the horseshoe vortex system wrapping around the roughness. As the vortices turn downstream the situation becomes that of a streamwise vortex in a shear layer, which is an extremely unstable situation. In addition, the unsteadiness occurring in the vortex system upstream of the roughness causes the disturbances to be sent downstream in the vortices. Second, as the flow travels around the cylinder it separates, forming a separation line around the roughness element from which forms a shear layer. This shear layer is susceptible to the Kelvin-Helmholtz inviscid instability and also has disturbances traveling in it from the unsteadiness upstream. These two downstream instabilities, the horseshoe vortex and the shear layer, are both cause the flow to begin to transition.

Effect of grid resolution:

The horseshoe vortex upstream requires some more attention. Prior to the simulations described in this chapter, the source of the disturbances was unknown to the experimenters. Being unable to measure in certain regions of the flow without disrupting the flow itself made this difficult to ascertain. However, simulations are able to unobtrusively probe the flow and so it was discovered that the source of the disturbances is the upstream vortex system becoming unsteady. With this information the experiment was redesigned to include surface pressure probes in the separation region. The CFD prediction was confirmed – the source of the disturbances is, in fact, the upstream vortex structure.

Initially, the grid on which these disturbances were found had a resolution of 24 points per diameter (D). The resulting unsteadiness had a peak in the frequency domain at 17 kHz. Unfortunately, the experiment found the peak frequency to be near 21 kHz. This

discrepancy of $\approx 20\%$ was thought to most likely be caused by grid resolution. To ensure that the flow is not being affected by the grid density and is truly a DNS, a grid resolution study was conducted. Condition I does not contain the 21 kHz instability according to experiment and was found to be steady according to CFD. Therefore, condition II was chosen to conduct the first grid resolution study. The 21 kHz instability is a fundamental feature of the flow and the simulations should be able to predict it.

Grids were made with an increasing resolution of 16, 24, 32 and 40 points per diameter and run on the smaller domain extending 10 diameters downstream. This resulted in grids of size 4 million, 13 million, 30 million and 70 million elements, respectively. A numerical probe is placed at the wall 1.5 D upstream of the element (distance is given with respect to the center of the roughness, thus 1 D upstream of the leading edge of the roughness). A numerical probe is simply the grid element closest to a given location. The solution in this element is written to a file after each iteration of the fluid solver. This is the location of one of the probes in the newly designed experiment making direct comparisons possible.

For condition II it was found that the lowest grid resolution (16 points per diameter) was not able to capture any physical unsteadiness. At 24 points per diameter unsteadiness was observed, but at 17 kHz. At both 32 and 40 points per diameter the peak moved to 21 kHz. This was taken to mean two things. First, the grid with a resolution of 32 points per diameter is grid resolved and more refined grids are unnecessary. Second, the simulation is able to correctly capture the physics of the flow and compute the correct fundamental frequency of this instability. Results are shown in Figure 5.6(a)

Computing the correct amplitude is also important for this flow. If both the frequency and amplitude of disturbances are correctly produced, it is likely that the flow can correctly be described as a DNS. Figure 5.6(b) shows the frequency content of the pressure fluctuations at the location $1.5D$ upstream of the roughness. There is very good agreement in the locations of the peaks as well as the amplitudes. The disagreement in the valleys between peaks is likely due to the level of background noise. In the experiment there is noise, albeit at a very low level, while in the computations there is no noise at all.

The same such as that of condition III, the frequency does not converge with the same resolution. Both 32 and 40 points per diameter resolutions under-predict the frequency at about 17-18 kHz while the experiment continues to see the 21 kHz frequency. It is unknown

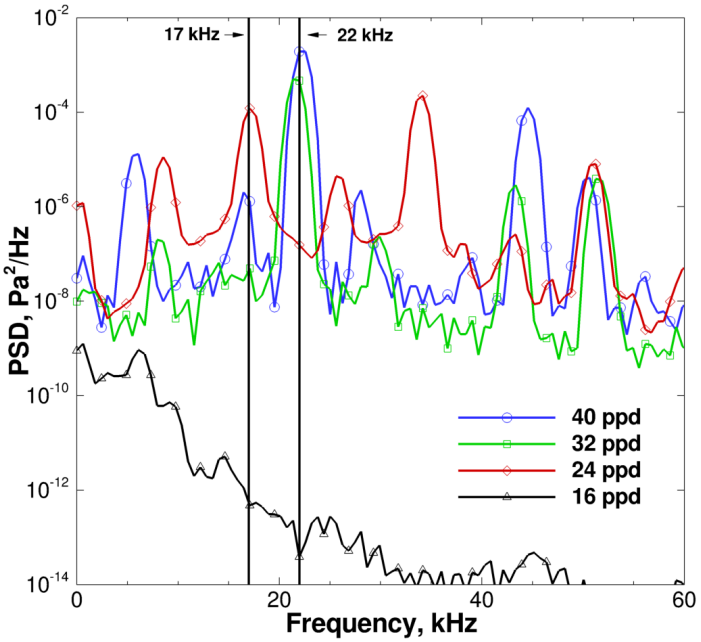

(a) Power spectrum density for several grid resolutions at $x_o = -1.5D$.

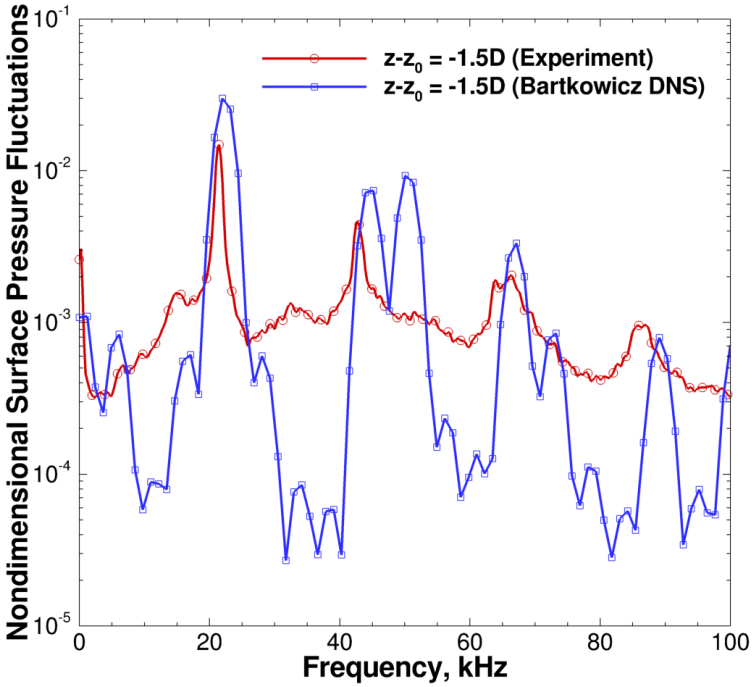

(b) Frequency content of pressure fluctuations at $x_o = -1.5D$.

Figure 5.6: For condition II there are 32 points per diameter required for grid convergence. At this resolution there is good agreement in both frequency and amplitude to experiment.

if increasing the grid density further would see the correct frequency or not as a density of 48 points per diameter would result in a 100 million element grid. This would be a massive simulation in itself, and if the results show this resolution is needed it would not be possible (with current resources) to simulate the large domain. It was decided instead to use the converged grid density for condition II as the results would still be physically meaningful even if the disturbance frequency is under-predicted by 20%.

Flow visualization:

Experimental results in the wake of the roughness element show that at the lowest Reynolds number the flow is laminar while the higher Reynolds number flows show signs of transition to turbulence. Figures 5.7 and 5.8 show a panoramic view of the flow structure for the three cases computed. Plotted are iso-surfaces of Q (described in the last chapter). The first image (condition I) contains a view closer to the roughness since there is not much else to see. Upstream are the very distinct horseshoe vortices wrapping around and turning downstream. Trailing the roughness are another set of vortices. These structures get weaker as they move downstream until they are no longer visible. Heat flux is also plotted on the surface in that figure and the effect the roughness has can be seen. Locally there are some augmented heat flux values, but they begin to quickly decay back to normal laminar levels.

Conditions II and III, however, are unsteady and disturbances created upstream can be seen convecting downstream and growing in both the shear layer and the horseshoe vortex. Condition II has disturbances with much smaller amplitudes created upstream and they take some time to grow downstream. Helical structures develop in the streamwise vortex and ring shaped structures form in the shear layer, due the shear layer being curved. Near the end of the domain the linear growth of the structures appears to suddenly change and grow much more chaotic, perhaps indicating the onset of transition.

The highest Reynolds number has much larger disturbances created upstream and they can be seen forming into helical structures almost immediately after passing the roughness and then quickly breaking down. The wake itself appears to be unsteady and though the ring shaped structures can still be seen, they begin to breakdown rapidly as well.

Planes in the streamwise direction can also illustrate the growth of the disturbances quite well. Figure 5.9 shows temperature contours along the symmetry plane as well as

perpendicular to that plane at a height $k/2$. Very small disturbances can be seen in the shear layer growing as they move downstream. Perpendicular to the symmetry plane shows the growth of the helical disturbances in the horseshoe vortex. They also appear to be growing very regularly until about $50D$ downstream where they begin to breakdown.

Similarly, Figure 5.10 shows the same plots for condition III. The symmetry plane does not show the slow, regular growth of the disturbances in the shear layer. Instead, the wake appears to be unsteady and begins to break down almost as soon as the shear layer can begin to roll-up. The same trend occurs in the perpendicular plane. Large disturbances are seen in the horseshoe vortex which appears to breakdown quickly and looks quite turbulent by the end of the domain.

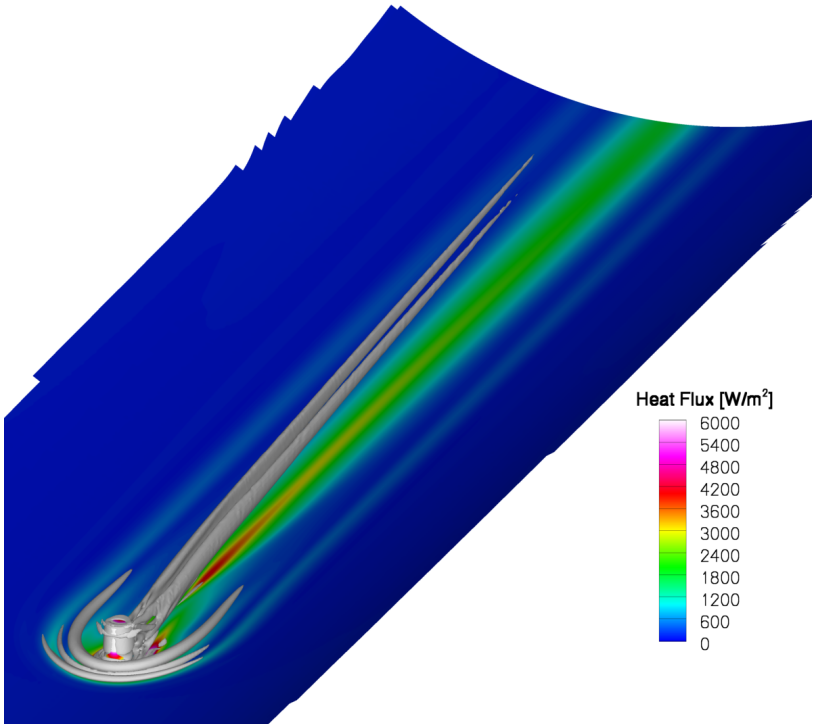

Figure 5.7: Horseshoe vortex structure and its effect on the heat flux can be seen clearly for condition I.

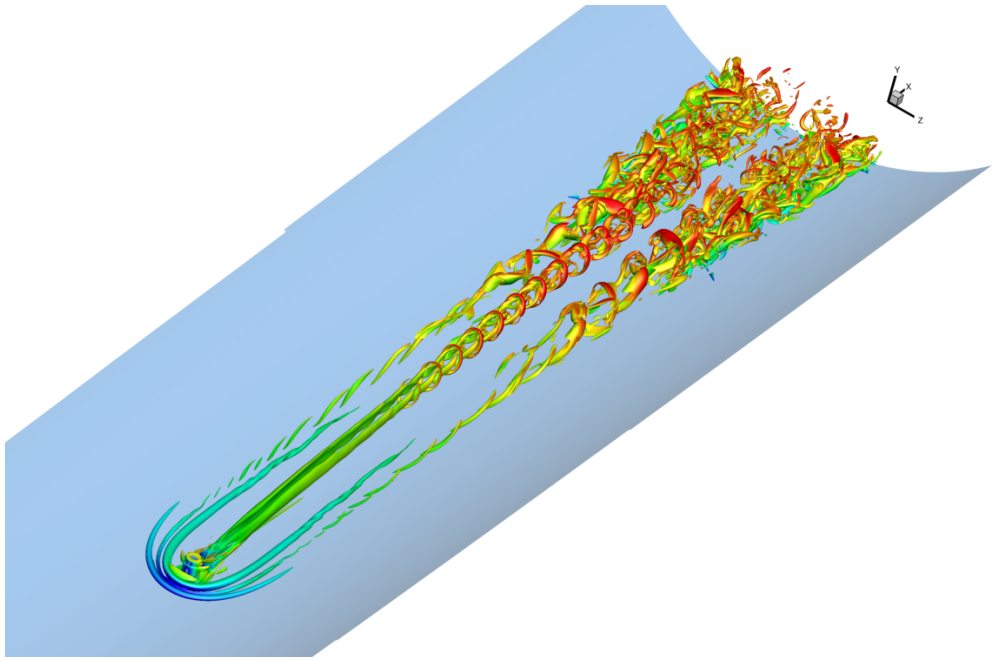

(a) Condition II ($p_\circ = 75$ psi).

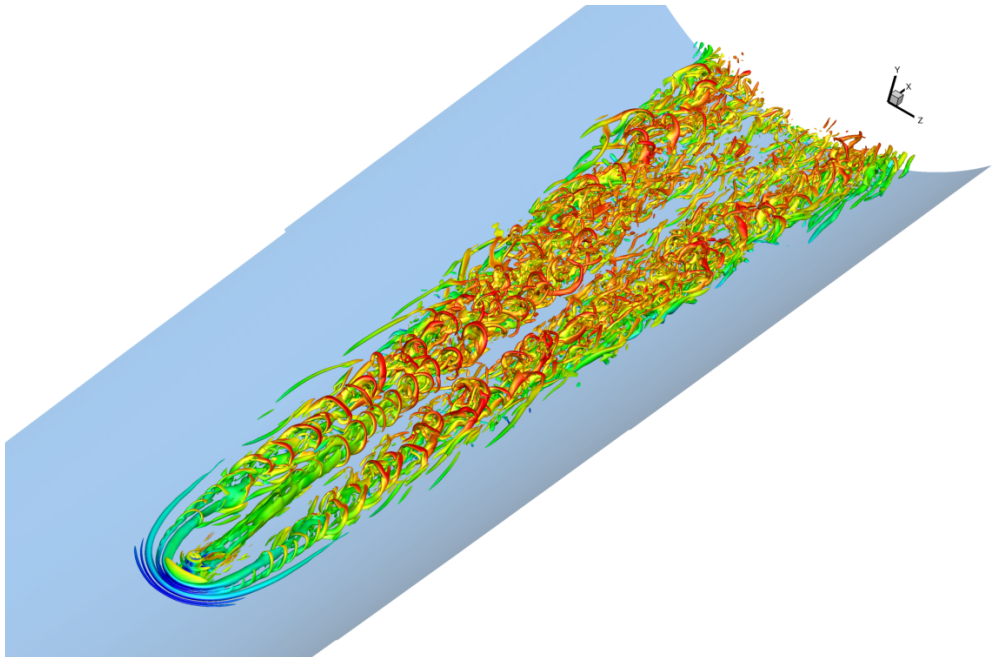

(b) Condition III ($p_\circ = 90$ psi).

Figure 5.8: Condition II develops helical structures that slowly grow while condition III quickly grows turbulent.

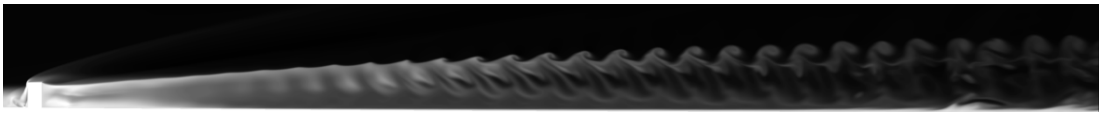

(a) Condition II ($p_\circ = 75$ psi) on the symmetry plane.

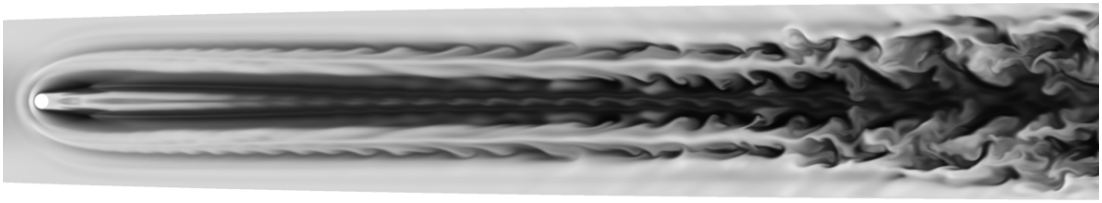

(b) Condition II ($p_\circ = 75$ psi) perpendicular to the symmetry plane.

Figure 5.9: Temperature contours show the slow growth of disturbances in the shear layer and in the horseshoe vortex before the structures finally break down.

(a) Condition III ($p_\circ = 90$ psi) on the symmetry plane.

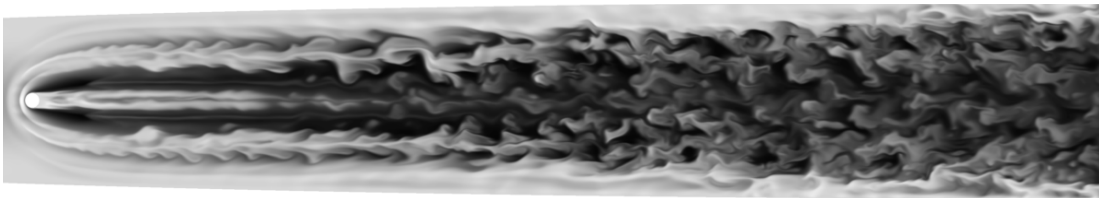

(b) Condition III ($p_\circ = 90$ psi) perpendicular to the symmetry plane.

Figure 5.10: Temperature contours show the quick breakdown of structure on both the shear layer and in the horseshoe vortex.

Flow analysis:

Unfortunately the wind tunnel in which these experiments were conducted cannot do much in the way of flow visualization to compare with the images just shown. Curved tunnel walls (and windows) preclude the use of Schlieren imaging and seeding the flow to perform particle image velocimetry (PIV) would disrupt the flow enough to make the experiment no longer useful.

Instead the focus in the experiment is on measuring the frequency and amplitude of disturbances. Previously the frequency of the instability was shown to match the experimentally measured frequency as long as sufficient grid resolution was achieved. The next question to answer is: How does the amplitude of the disturbance compare to the experiment, both in the separation region upstream and far downstream where the flow has begun to transition or turned turbulent?

In the upstream region Figure5.6(b) shows that condition II predicts the amplitude of the disturbance quite well. Because condition III doesn't match the frequency quite as well (18 kHz vs. 21 kHz) a slightly different analysis was done to compare the amplitudes. At $x = -1.5D$ the power spectral density was integrated across the instability. The experiment's frequency integration range was 18-25 kHz while CFD integrate over the range from 15-22 kHz. The result is that the RMS pressure fluctuations, normalized by the mean pressure, are 6.6% for the experiment vs. 6.4% for the CFD.

A set of pressure measurements at various points on the wall were available to compare to experimental results. The computational domain extends a distance of $75D$ downstream. Within this domain there are three downstream sensors at 21.9, 46.3 and $63.3D$. Several different runs were performed with the sensors placed 0.0, 1.0 and $2.0D$ off the centerline. There are also data from three sensors near the roughness at 0.0 and $2.0D$ off the centerline.

Figures 5.11 and 5.12 attempt to compare all the sensor data to CFD results simultaneously. To compare all the data on the surface, the tunnel wall is plotted as the x-z plane with the pressure fluctuations plotted on the vertical axis. Very good agreement is reached between the experiment and simulations.

Statistics were taken for roughly 250 flow times (based on the ratio of the roughness diameter and the freestream velocity) for condition II and 600 flow times for condition III.

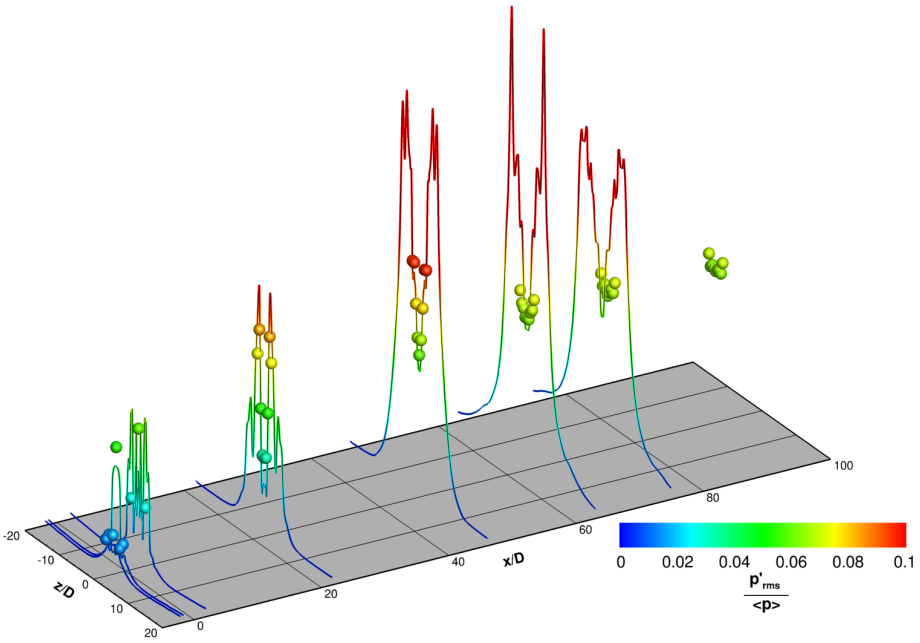

(a) Condition II ($p_\circ = 75$ psi) pressure fluctuations on the whole domain.

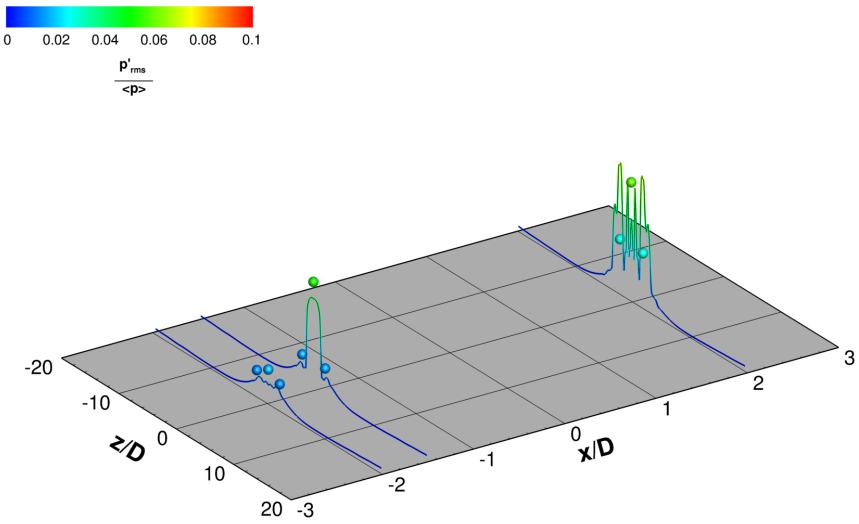

(b) Condition II ($p_\circ = 75$ psi) pressure fluctuations near the roughness.

Figure 5.11: The tunnel wall has been unrolled onto the x-z plane. The y-axis as well as the contour colors represent the pressure fluctuations. Lines represent the CFD data; the dots represent the experimental data.

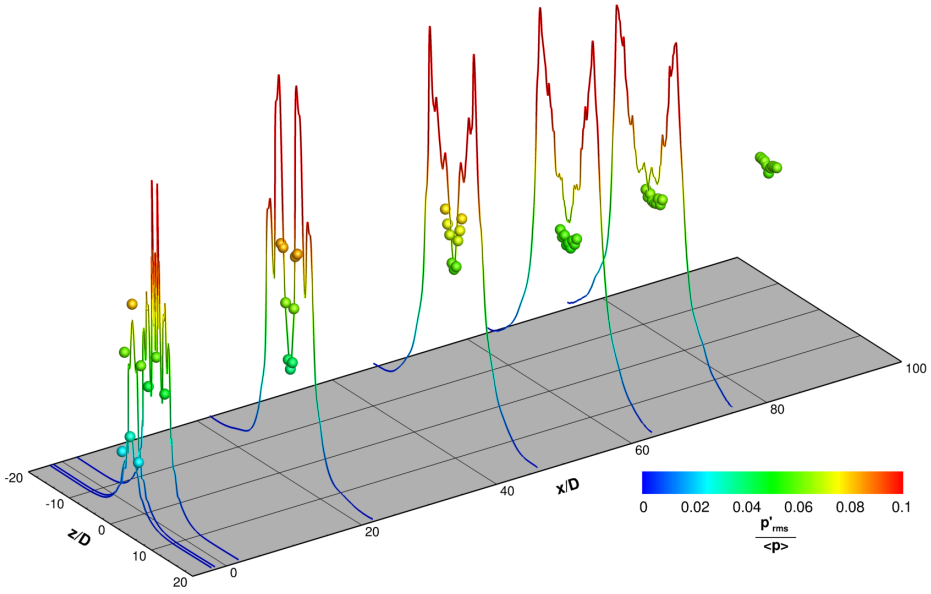

(a) Condition III ($p_\circ = 90$ psi) pressure fluctuations on the whole domain.

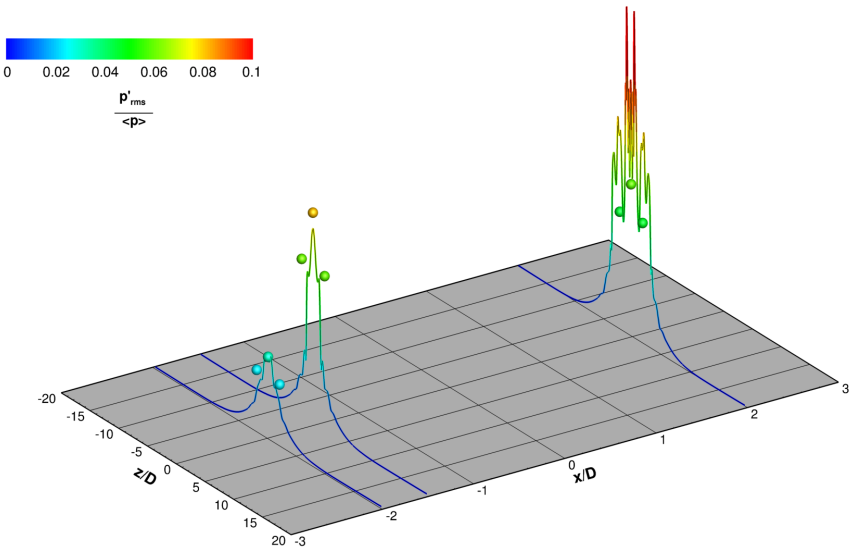

(b) Condition III ($p_\circ = 90$ psi) pressure fluctuations near the roughness.

Figure 5.12: The tunnel wall has been unrolled onto the $x - z$ plane. The y-axis as well as the contour colors represent the pressure fluctuations. Lines represent the CFD data; the dots represent the experimental data.

At 0.0, 1.0 and 2.0 D off the centerline (Figure 5.13) the agreement is very good, especially on the symmetry plane. There are fewer experimental probes available for comparison off the centerline, but the existing probes agree well. The simulations over predict the pressure fluctuations very slightly. This may be due to the fact that the experimental and numerical flow conditions are not exactly the same; condition III is compared to an experiment with a stagnation pressure of 85 psi while condition II is compared to an average of experiments with stagnation conditions of 75 psi and 80 psi.

Off the centerline is where the flow seems to be transitioning the quickest, due to the horseshoe vortex. At $1D$ off the centerline condition II has a peak in the pressure fluctuations before beginning to drop again around $50D$ downstream. This is very indicative of transition. Similarly for condition III, at $2D$ off the centerline there is a peak in the fluctuations at around $25D$ downstream before quickly dropping. Unfortunately, the experimental probes are placed on each side of the peaks in both cases, so it's difficult to say with certainty if the transition is indeed occurring at those locations. However, in the CFD this seems to be the case. By examining boundary layer profiles it will be more clear if the boundary layer has transitioned.

If the boundary layer is becoming fully turbulent (condition III) or just transitioning (condition II), then Van Driest transformed boundary layer profiles (Equation 5.1) should begin to collapse to the classic turbulent boundary layer profile. A classical flat plate boundary layer profile will follow $u^+ = y^+$ in the near wall region and $u^+ = \frac{1}{0.41}\log(y^+)+5.1$ in the outer region of the boundary layer. Surface pressure fluctuations seemed to indicate that condition II began to transition near the end of the domain, about $50D$ downstream of the roughness. Figure 5.14 shows boundary layer profiles from $20D$ to $70D$ downstream at $1D$ off the centerline (for condition II). At first the boundary layer aligns well with the laminar profile ($u^+ = y^+$) with slight distortion from the roughness. Further downstream the profiles begin to move towards the turbulent profile, but never quite collapses completely, indicating the profiles are most likely still transitional. Figure 5.14 also shows the same profiles for condition III, but $2D$ off the centerline. Surface pressure fluctuations indicated that this boundary layer began to transition near $25D$. Profiles for this case quickly collapse

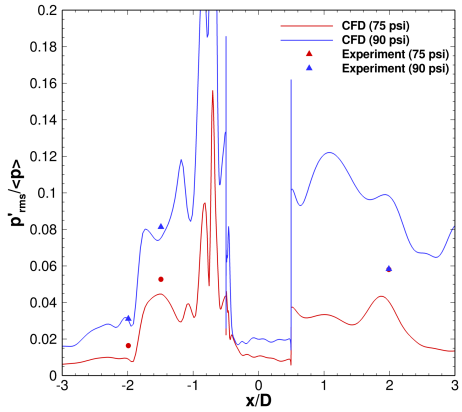

(a) Surface pressure fluctuations on the centerline near the roughness.

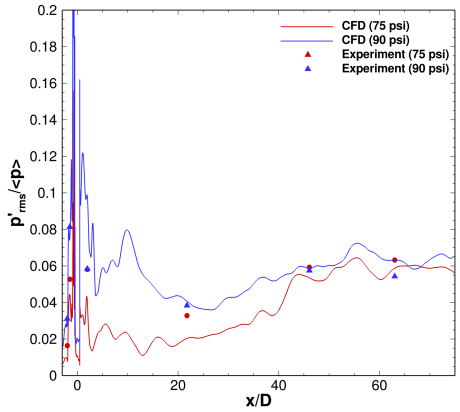

(b) Surface pressure fluctuations on the centerline for the entire domain.

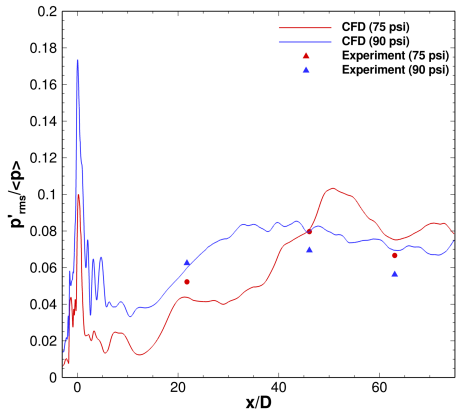

(c) Surface pressure fluctuations $1.0D$ off the centerline.

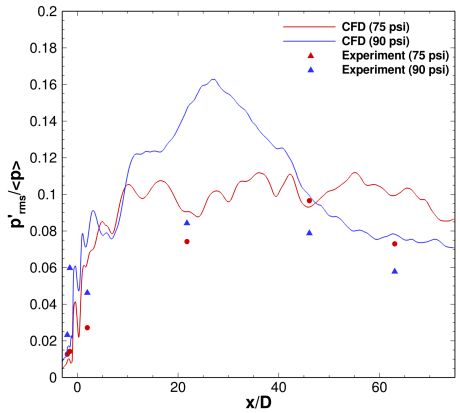

(d) Surface pressure fluctuations $2.0D$ off the centerline.

Figure 5.13: Surface pressure fluctuations normalized by mean pressure at several locations from the centerline.

to the classical turbulent boundary layer profile, indicating that this flow is fully turbulent.

$$u_{\text{VanDriest}}(y) = \int_0^{u(y)} \sqrt{\frac{\rho}{\rho_w}}\ \mathrm{d}u \tag{5.1}$$

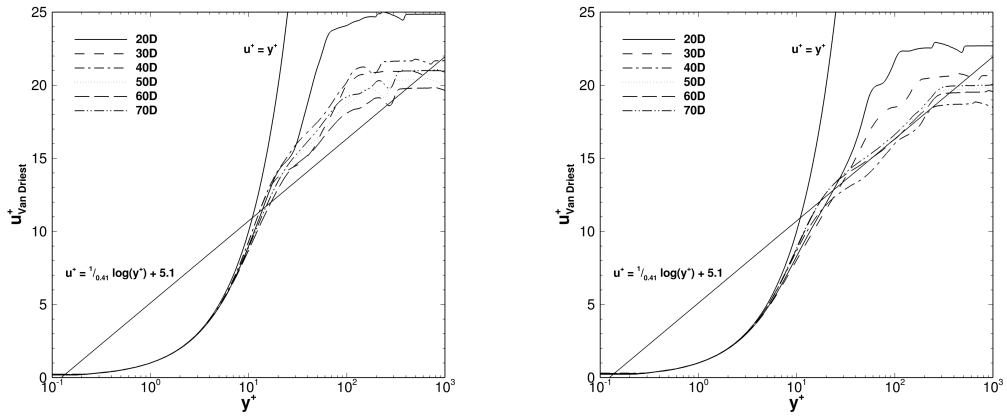

(a) Boundary Layer profiles $1D$ off centerline for condition II.

(b) Boundary Layer profiles $2D$ off centerline for condition III.

Figure 5.14: Van Driest transformed boundary layer profiles at several streamwise locations. Transformed velocity is normalized by u_τ. Wall distance is plotted in wall units (y^+).

Figure 5.15 shows the Reynolds stresses $70D$ downstream and $2D$ off centerline for condition III. Symbols in this plot are from Spalart (1988) data from a DNS of a turbulent incompressible boundary layer on a flat plate. In the near wall region the peaks in the Reynolds stresses match the Spalart data well: u' slightly over predicts the peak while v' and w' slightly under predict their respective peaks. In the outer region of the boundary layer all three slightly over predict the Spalart data. This may be due to the three dimensionality of the boundary layer.

5.4.2 Variable Roughness Height : k = 7.4 - 11.2 mm

The previous section has concerned instabilities occurring due to a fixed roughness height of 10.2 mm and the corresponding instability mechanism developing in the upstream separation region when p_o is varying. This section will explore the effect of roughness height on the instability mechanism and the downstream wake for a fixed stagnation pressure of $p_o = 90$ psi. At this stagnation pressure, the undisturbed boundary layer thickness (δ) at

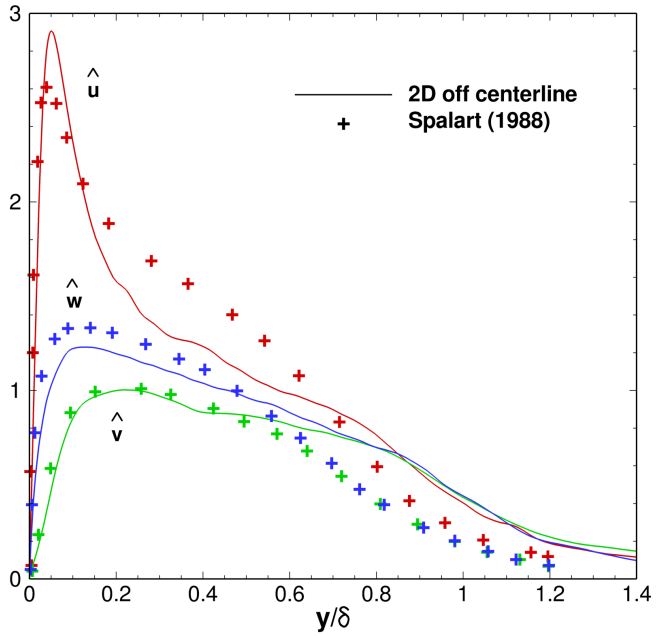

Figure 5.15: Turbulence intensities at $70D$ downstream and $2D$ off the centerline. Solid lines are from the current work with $\hat{u}_i = \sqrt{\frac{\rho}{\rho_w}}\frac{u'_{i,rms}}{u_\tau}$, data points are from Spalart (1988) with $\hat{u}_i = \frac{u'_{i,rms}}{u_\tau}$.

the location of the roughness is approximately 8.3 mm. Computations were performed for roughness heights of 7.4, 7.9, 8.4, 9.1, 10.2 and 11.2 mm as presented in Table 5.2.

Table 5.2: Simulation Parameters; $p_o = 90$ psi

k [mm]	k/δ	Re_k
7.366	0.89	2.7×10^4
7.874	0.95	4.1×10^4
8.382	1.01	5.3×10^4
9.144	1.10	6.2×10^4
10.2	1.23	7.0×10^4
11.176	1.35	7.7×10^4

Previous experimental work for a fixed roughness height of 10.2 mm observed a change in the dominant instability as the tunnel Reynolds number was varied (Chou et al. (2011)). At values of Re_k above approximately 5×10^4, the dominant instability occurred at a frequency near 21–22 kHz and was verified in computations. The frequency of this instability was not observed to vary greatly with Reynolds number. Below $Re_k \approx 5 \times 10^4$, the experiment found the dominant instability occurred at higher frequencies of 40–70 kHz and had a frequency that varied greatly with Reynolds number. As the Reynolds number decreased, the frequency of the higher-frequency instability also decreased. This second instability was never observed in the computations, which showed steady flow at the conditions of the experiments. Both types of instabilities were observed experimentally to occur upstream of the roughness within the separation region. Based on the results for a constant roughness height, a similar change in transition mechanism would be expected for a constant Reynolds number as the roughness height (and thus Re_k) is reduced.

The grids for these simulations extend upstream to $x/D = -25$ and downstream to $x/D = 10$ to maintain manageable grid sizes and maximize the number of cases that could be simulated. These smaller grids seemed to be justified for these cases as experimental results showed the flow transitioning shortly downstream of the roughness, with the mechanism for transition existing in the separation upstream of the roughness.

Figure 5.16 shows iso-surfaces of the 'Q' criterion colored by the local non-dimensional velocity. In the case of the k =11.2 mm roughness the disturbances created by the oscillations of the separation region can clearly be seen as hairpin shaped vortical structures convecting downstream in the horseshoe vortex. These disturbances are also seen in the

wake directly behind the roughness element where the flow looks to be very unsteady. For the k =10.2 mm roughness height, the main difference appears to be the width of the horseshoe vortex. This is most likely due to differences in the bow shock off the leading upper edge of the roughness. As the height is lowered, less of the element is exposed to the supersonic freestream. This results in less of the high pressure region that turns the flow back upstream into the separation region. For this height, disturbances in both the horseshoe vortex and wake are still visible.

As the height is further reduced to 9.1 mm, the width of the horseshoe vortex is also reduced. The disturbances can still be seen in the horseshoe vortex, but the wake appears to be laminar – or nearly so. At k =8.4 mm the horseshoe appears to be significantly weaker and the size of disturbances in this region are much smaller. The wake appears to be more steady as well.

In the two lowest heights the wakes appear to be completely laminar. Although the heights remain above the sonic line, the normal shock created has continually weakened. This results in the horseshoe vortices becoming weaker as well. The k =7.9 mm roughness continues to show very small disturbances in the horseshoe vortex while the shortest height, k =7.4 mm, is completely laminar and steady.

Figure 5.17 shows the RMS surface pressure along the centerline for each case, just upstream and downstream of the roughness. Experimental measurements are plotted as colored dots for comparison. The pressure fluctuations decreases as the height is reduced; this trend was observed in both CFD and experiment. In addition, as the height is reduced the extent of the separation region grows smaller and moves closer to the upstream edge of the roughness.

Spectra from the experimental surface-pressure measurements at $x = -1.5D$ were compared to CFD time-history data from the same location, in an effort to observe the change in the dominant instability mechanism as the roughness height is reduced. The CFD data were a time-average from five probes across the area of the experimental sensor face (CFD 'probes' are time histories of the solution in a grid element. Because the sensors are larger than the grid elements, several of these grid elements are averaged to approximate the actual sensor).

A comparison of experimental and computational spectra for five roughness heights is

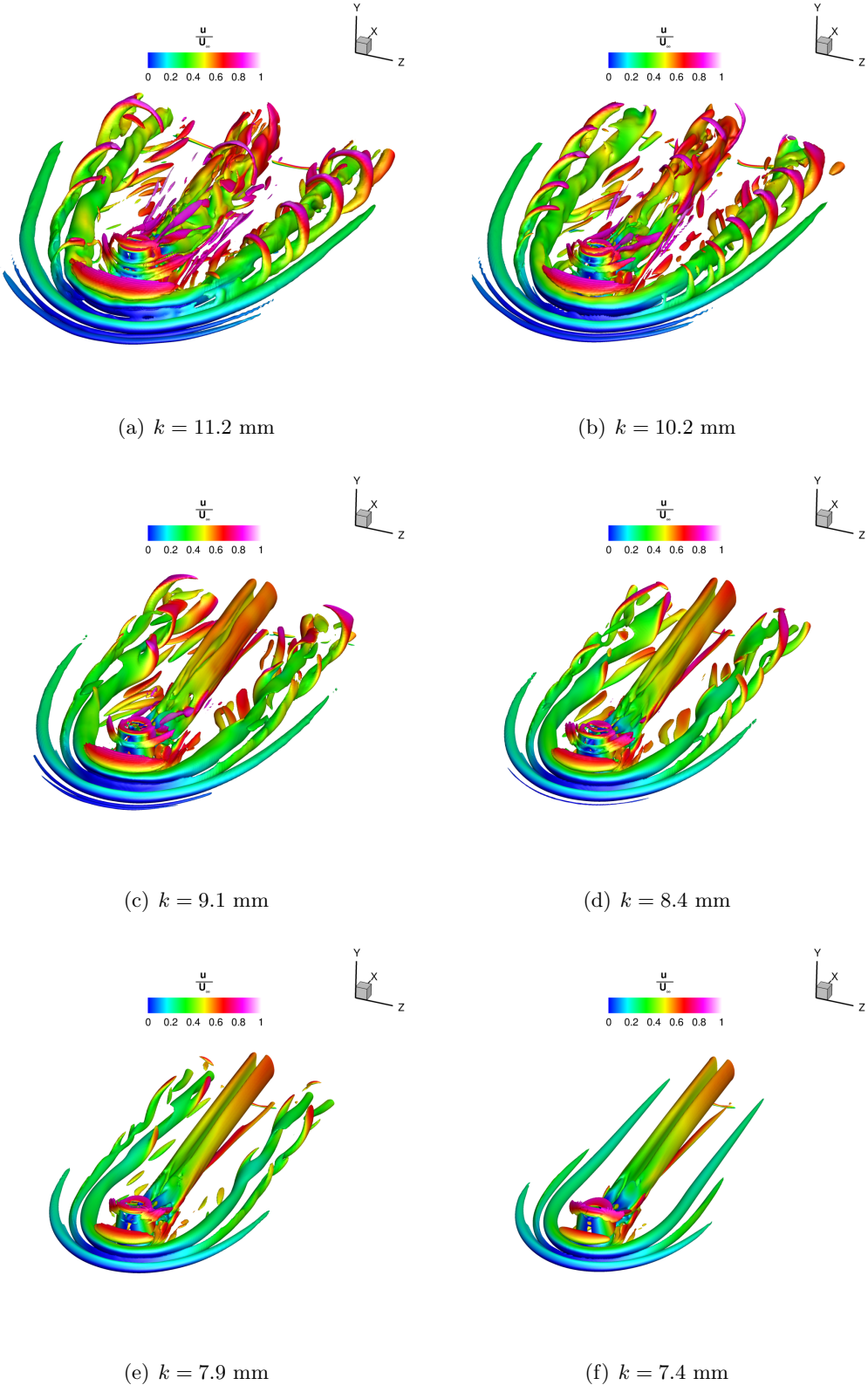

(a) $k = 11.2$ mm

(b) $k = 10.2$ mm

(c) $k = 9.1$ mm

(d) $k = 8.4$ mm

(e) $k = 7.9$ mm

(f) $k = 7.4$ mm

Figure 5.16: Iso-surfaces of 'Q' for each roughness height.

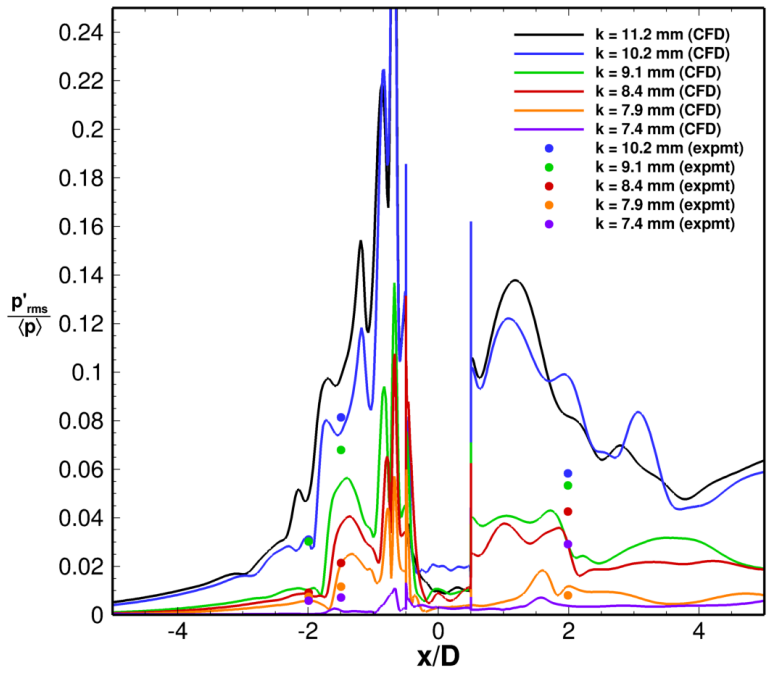

Figure 5.17: Computed and measured RMS pressure for various roughness heights at the surface along the centerline. As the height decreases, the general trend is for the fluctuations to also decrease. Agreement upstream of the roughness is quite good with less agreement downstream.

shown in Figure 5.18. Note that no experimental data were available for the k =11.2 mm case. Smooth-wall laminar and turbulent spectra obtained from the experiments are also plotted. The laminar spectrum shows approximate noise levels in the experiments. The noise levels in the experiments are higher than in the computations since freestream noise effects were not simulated. The experimental trends are the same as a constant roughness height with decreasing freestream Reynolds number: as the roughness height is reduced, the instability near 21–22 kHz disappears and a new higher-frequency instability appears as broadband fluctuation levels are reduced. As the height is reduced from k =10.2 mm to k =8.4 mm the instability frequency increases by roughly 4 kHz and the amplitude decreases slightly. A similar trend is observed in the computations. In the computations, as the roughness height is reduced the peak frequency increases from 18 kHz to 25 kHz and the amplitude of the peak decreases. At the largest roughness heights of k =10.2 mm and k =11.2 mm, the spectra from both experiment and computation are near the smooth-wall turbulent amplitudes. However, as the roughness height is reduced the main instability peak near 18–25 kHz does not disappear in the computations until k =7.4 mm. Instead, the peak remains along with harmonics as the broadband fluctuations decrease below the experimental noise levels.

A detailed comparison of the spectra shows that good agreement of the dominant instability in the separation region is obtained for the larger roughness heights (Figure 5.18). When k =10.2 mm the fluctuations are near smooth-wall turbulent levels. The peak frequencies as well as the harmonic frequencies show slight disagreement. When k =9.1 mm the broadband noise of the computations decreases below the experimental noise floor, but the peaks and harmonics remain strong. An additional peak is seen at 5 kHz, but is not as strong as the 22-kHz peak. The 22-kHz peak and harmonics remain strong when k =8.4 mm, though several other peaks appear in the experiment that are not seen in the computations. When k =7.9 mm, good agreement was not obtained for unknown reasons. At this height, the peak near 21–22 kHz disappears completely from the experiment and a new peak at 50 kHz appears along with a harmonic. In the computations, however, a large peak near 25 kHz is still visible. Finally, when k =7.4 mm both experiment and computation show steady flow at $x = -1.5D$.

The differences between experiment and CFD are likely due to freestream noise effects

that are not present in the simulations. It is possible that the large instability near 21–22 kHz occurring at higher roughness heights is not sensitive to external disturbances and is an absolute-type instability. The instability at higher frequencies (occurring for lower roughness heights) could be more sensitive to external disturbances that cause it to grow to large levels in the experiments.

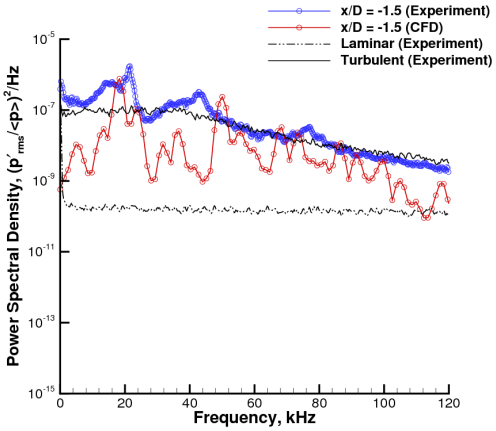

(a) $k = 10.2$ mm, k/δ=1.23, $Re_k = 7.0 \times 10^4$

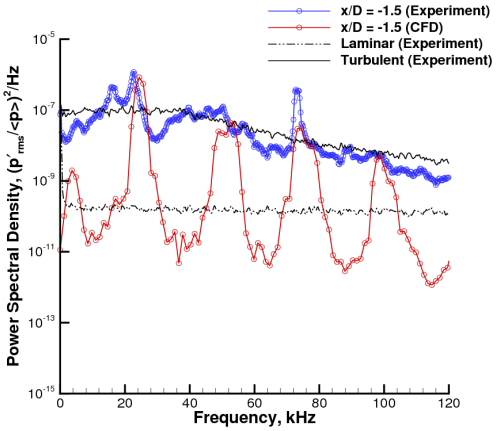

(b) $k = 9.1$ mm, k/δ=1.10, $Re_k = 6.2 \times 10^4$

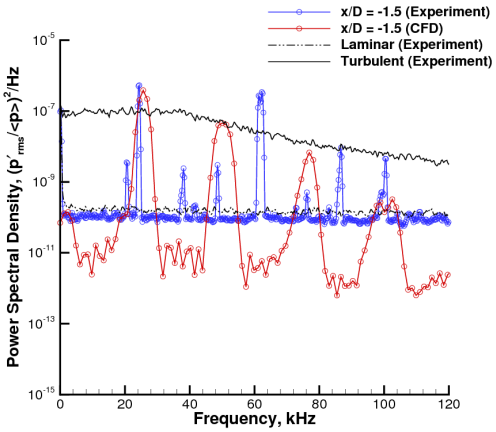

(c) $k = 8.4$ mm, k/δ=1.01, $Re_k = 5.3 \times 10^4$

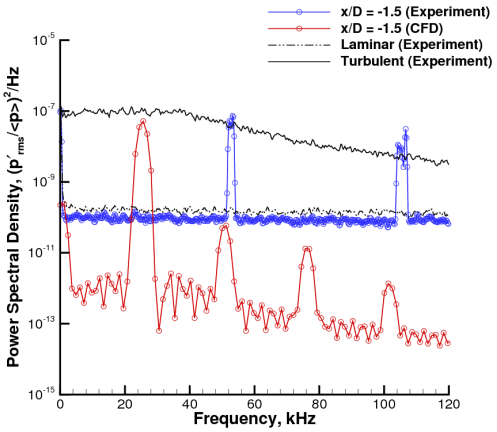

(d) $k = 7.9$ mm, k/δ=0.95, $Re_k = 4.1 \times 10^4$

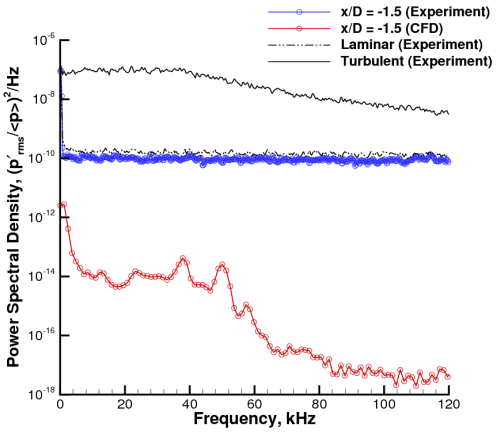

(e) $k = 7.4$ mm, k/δ=0.89, $Re_k = 2.7 \times 10^4$

Figure 5.18: Spectra at $x/D = -1.5$ showing the effect of roughness height on instabilities in the upstream separation region.

Chapter 6

Summary and Conclusions

In this dissertation a method for obtaining higher order accurate inviscid fluxes has been presented. The method works in the context of unstructured grids which contain hexahedral cells (bricks). Both a fourth and sixth order accurate (in space) method was put forth. Using the gradient reconstruction method in conjunction with low-dissipation fluxes has allowed for the computation of problems which normally would require an inordinate amount of grid points. Obtaining the fluxes only requires a linear combination of data from nearby cells, resulting in a negligible increase in computation time.

The method was applied to one of the problems at the forefront of hypersonic flight research: boundary layer transition. A model of acoustic noise was used to simulate an elliptic cone with a noisy freestream. The growth of this noise was observed in the boundary layer which eventually led to a breakdown and transition. The growth was only possible with the low-dissipation and higher order numerics, without which numerical viscosity would have damped out all unsteadiness. For the conditions simulated the conclusion is that at low Reynolds numbers the centerline begins to transition. However, as the Reynolds number is increased the crossflow vortices quickly begin to transition, creating secondary disturbances which get radiated into the centerline boundary layer.

Roughness induced transition was also simulated using the advancements in numerics. An instability was observed in the separation region created by a cylindrical roughness element. The first qualitative comparison between experiment and CFD was made for an instability of this kind and found to agree very well. The low-dissipation numerics and sixth order accurate fluxes were found to be vital to the success of the simulation. Without the low-dissipation no instability was observed. Without the sixth order fluxes the structures

created by the instability were not well resolved. Downstream of the roughness the boundary layer was found to become turbulent which is in agreement with the experimental results.

Because the inertia is so dominant over viscous forces in high Reynolds number flows, this work focused on the inviscid fluxes. However, transition of boundary layers is necessarily in regions near the wall where viscous fluxes become very large. The extension of the gradient reconstruction method to viscous fluxes is presented in the appendix to this work. Implementation and testing needs to be done to determine if there are any unforeseen difficulties.

The method assumes a Cartesian grid and is formally higher order accurate in this special case. Although it was shown that the method works very well, even on non-Cartesian grids, some effort should be put into quantifying the error for non-ideal grids. Also, it may be possible to extend the method to include the locally varying geometry. As such, it shows promise for improvement.

References

[1] Sigal Gottlieb and Chi-Wang Shu. Total Variation Diminishing Runge-Kutta Schemes. *Mathematics of Computation*, 67(221):73–85, January 1998.

[2] J. L. Steger and R. F. Warming. Flux Vector Splitting for the Inviscid Gasdynamic Equations with Application to Finite-Difference Methods. *Journal of Computational Physics*, 40(1):263–293, 1981.

[3] L. M. Mack. Boundary-layer linear stability theory. Special Course on Stability and Transition of Laminar Flow, AGARD Report No. 709, 1984.

[4] A. S. W. Thomas. Physics of Fluids. *The unsteady characteristics of laminar juncture flow*, 30(2), 1966.

[5] I. Tani, H. Komoda, Y. Komatsu, and M. Iuchi. Boundary-Layer Transition by Isolated Roughness. Aeronautical Research Institue, University of Tokyo, Report No. 375, 1962.

[6] Y. A. Panov and A. I. Shvets. Pressure Oscillation on a Plane Upstream of an Obstacle in Supersonic Flow. *Fluid Dynamics*, 33(1):56–60, 1998.

[7] D. M. Voitenko, A. I. Zubkov, and Yu. A. Panov. Supersonic Gas Flow Past a Cylindrical Obstacle on a Plate. *Mekhanika Zhidkosti i Gaza*, 1(1):121–125, 1966.

[8] Amanda Chou, Bradley M. Wheaton, Christopher A. C. Ward, Peter L. Gilbert, Laura E. Steen, and Steven P. Schneider. Instability and Transition Research in a Mach-6 Quiet Tunnel. AIAA Paper 2011-283, January 2011.

[9] Eli Reshotko and Anatoli Tumin. Role of Transient Growth in Roughness-Induced Transition. *AIAA Journal*, 42(4):766–770, April 2004.

[10] M. S. Acarlar and C. R. Smith. A Study of Hairpin Vortices in a Laminar Boundary Layer. Part 1. Hairpin Vortices Generated by a Hemisphere Protuberance. *Journal of Fluid Mechanics*, 175:1–41, 1987.

[11] R. L. Kimmel, J. Poggie, and S. N. Schwoerke. Laminar-Turbulent Transition in a Mach 8 Elliptic Cone Flow. *AIAA Journal*, 37:1080–1087, 1999.

[12] J. Poggie, R. L. Kimmel, and S. N. Schwoerke. Traveling Instability Waves in a Mach 8 Flow over an Elliptic Cone. *AIAA Journal*, 38:251–258, 2000.

[13] R. D. Joslin. Evolution of Stationary Crossflow Vortices in Boundary Layers on Swept Wings. *AIAA Journal*, 7:1279–1285, 1995.

[14] R. D. Joslin and C. L. Streett. The role of stationary cross-flow vortices in boundary-layer transition on swept wings. *Physics of Fluids*, 6:3442–3453, 1994.

[15] M. Huntley and A. Smits. Transition studies on an elliptic cone in Mach 8 flow using Filtered Rayleigh Scattering. *European Journal of Mechanics B/Fluids*, 19:695–706, 2000.

[16] M. B. Huntley. *Transition on Elliptic Cones at Mach 8*. PhD thesis, Princeton University, 2000.

[17] K. T. Berger, S. J. Rufer, R. Kimmel, and D. Adamaczak. Aerothermodynamic Characteristics of Boundary Layer Transition and Trip Effectiveness of the HIFiRE Flight 5 Vehicle. AIAA Paper 2009-4055, 2009.

[18] C. R. Alba, H. B. Johnson, M. D. Bartkowicz, G. V. Candler, and K. T. Berger. Boundary-Layer Stability Calculations for the HIFiRE-1 Transition Experiment. *Journal of Spacecraft and Rockets*, 45, 2008.

[19] M. S. Holden, T. P. Wadhams, M. MacLean, and E. Mundy. Review of Studies of Boundary Layer Transition in Hypersonic Flows Over Axisymmetric and Elliptic Cones Conducted in the CUBRC Shock Tunnels. AIAA Paper 2009-782, 2009.

[20] S. L. Huang, G. K. Stuckert, and T. Herbert. Cross Flow Instability of the Supersonic Flow over a 4:1 Elliptic Cone. ADOS Report, 1995.

[21] V. Daru and C. Tenaud. Evaluation of TVD high resolution schemes for unsteady viscous shocked flows. *Computers and Fluids*, 30:89–113, 2000.

[22] H. C. Yee and B. Sjögreen. Designing Adaptive Low-Dissipative High Order Schemes For Long-Time Integrations. *Turbulent Flow Computation*, 66:141–198, 2004.

[23] H. G. Hornung, P. H. Adam, P. Germain, K. Fujii, and A. Rasheed. On Transition And Transition Control In Hypervelocity Flow. Proceedings of the Ninth Asian Congress of Fluid Mechanics, 2002.

[24] P. T. Greene, J. D. Eldredge, X. Zhong, and J. Kim. A Numerical Study of Purdue's Mach 6 Tunnel with a Roughness Element. AIAA Paper 2009-0174, 2009.

[25] B. Thwaites. Incompressible Aerodynamics. Oxford University Press, 1960.

[26] S. P. Schnedier. Design of a Mach-6 quiet-flow wind-tunnel nozzle using the e**N method for transition estimation. AIAA Paper 98-0547, 1998.

[27] S. P. Schnedier. The Development of Hypersonic Quiet Tunnels. AIAA Paper 2007-4486, 2007.

[28] Hans W. Liepmann and Gertrude H. Fila. Investigations of Effects of Surface Temperature and Single Roughness Elements on Boundary-Layer Transition. NACA Report 890, 1947.

[29] C. J. Baker. The Laminar Horseshoe Vortex. *Journal of Fluid Mechanics*, 95:347–367, 1979.

[30] D. J. Maull. Hypersonic flow over axially symmetric spike bodies. *Journal of Fluid Mechanics*, 8:584–592, 1960.

[31] P. R. Spalart. Direct Simulation of a Turbulent Boundary Layer up to $R_\theta = 1440$. *Journal of Fluid Mechanics*, 187:61–98, 1988.

[32] J. Murlis, H. M. Tsai, and P. Bradshaw. The Structure of Turbulent Boundary Layers at Low Reynolds Numbers. *Journal of Fluid Mechanics*, 122:13–56, 1982.

[33] Ioannis Nompelis, Travis W. Drayna, and Graham V. Candler. A Parallel Unstructured Implicit Solver for Reacting Flow Simulation. AIAA Paper 2005-4867, 2005.

[34] Pramod K. Subbareddy and Graham V. Candler. A Fully Discrete, Kinetic Energy Consistent Finite-Volume Scheme for Compressible Flows. *Journal of Computational Physics*, 228:1347–1364, 2009.

[35] Michael J. Wright, Graham V. Candler, and M. Prampolini. Data Parallel Lower-Upper Relaxation Method for the Navier-Stokes Equations. *AIAA Journal*, 34:1371–1377, 1996.

[36] Daniel Feszty, Ken J. Badcock, and Bryan E. Richards. Driving Mechanisms of High-Speed Unsteady Spiked Body Flows, Part 1: Pulsation Mode. *AIAA Journal*, 42:95–106, 2004.

[37] F. Ducros, V. Ferrand, F. Nicoud, C. Weber, D. Darracq, C. Gacherieu, and T. Poinsot. Large-Eddy Simulation of Shock/Turbulence Interaction. *J. Comp. Phys.*, 152:517–549, 1999.

[38] Y. Ren M. Liu and H. Zhang. A Characteristic-Wise Hybrid Compact-WENO Scheme for Solving Hyperbolic Conservation Laws. *J. Comp. Phys.*, 192:365–386, 2003.

[39] Patrick Huerre and Peter A. Monkewitz. Local and Global Instabilities in Spatially Developing Flows. *Annual Review of Fluid Mechanics*, 22:473–537, 1990.

[40] R.L. Simpson. Junction Flows. *Annual Review of Fluid Mechanics*, 33:415–443, 2001.

[41] Bradley M. Wheaton, Steven P. Schneider, Matthew D. Bartkowicz, Pramod K. Subbareddy, and Graham V. Candler. Numerical and Experimental Comparison of Roughness-Induced Instabilities at Mach 6. Submitted to 41st AIAA Fluid Dynamics Conference and Exhibit, Honolulu, HI, June 2011.

[42] Brett F. Bathel, Paul M. Danehy, Jennifer A. Inman, A. N. Watkins, Stephen B. Jones, William E. Lipford, Kyle Z. Goodman, Christopher B. Ivey, and Christopher P. Goyne.

Hypersonic Laminar Boundary Layer Velocimetry with Discrete Roughness on a Flat Plate. AIAA Paper 2010-4998, June 2010.

[43] Prahladh S. Iyer, Suman Muppidi, and Krishnan Mahesh. Transition of Hypersonic Flow past Flat Plate with Roughness Elements. AIAA Paper 2010-5015, June 2010.

[44] Michael A. Kegerise, Lewis R. Owens, and Rudolph A. King. High-Speed Boundary-Layer Transition Induced by an Isolated Roughness Element. AIAA Paper 2010-4999, June 2010.

[45] Christopher A. C. Ward, Bradley M. Wheaton, Amanda Chou, Peter L. Gilbert, Laura E. Steen, and Steven P. Schneider. Boundary-Layer Transition Measurements in a Mach-6 Quiet Tunnel. AIAA Paper 2010-4721, June 2010.

[46] Matthew D. Bartkowicz, Pramod K. Subbareddy, and Graham V. Candler. Numerical Simulations of Roughness Induced Instability in the Purdue Mach 6 Wind Tunnel. AIAA Paper 2010-4723, June 2010.

[47] John Laufer, John E. F. Williams, and Stephen Childress. Mechanism of Noise Generation in the Turbulent Boundary Layer. AGARDograph 90, November 1964.

[48] Ulrich Rist and Anke J ager. Unsteady Disturbance Generation and Amplification in the Boundary-Layer Flow Behind a Medium-Sized Roughness Element. Sixth IUTAM Symposium on Laminar-Turbulent Transition, 293-298, 2006.

[49] P. M. Danehy, C. B. Ivey, J. A. Inman, B. F. Bathel, S. B. Jones, A. C. McCrea, N. Jiang, M. Webster, W. Lempert, J. Miller, and T. Meyer. High-Speed PLIF Imaging of Hypersonic Transition over Discrete Cylindrical Roughness. AIAA Paper 2010-703, January 2010.

[50] Meelan Choudhari, Fei Li, Minwei Wu, Chau-Lyan Chang, and Jack Edwards. Laminar-Turbulent Transition Behind Discrete Roughness Elements in a High-Speed Boundary Layer. AIAA Paper 2010-1575, January 2010.

[51] Seokkwan Yoon, Michael D. Barnhardt, and Graham V. Candler. Simulations of High-Speed Flow over an Isolated Roughness. AIAA Paper 2010-1573, January 2010.

[52] Matthew D. Bartkowicz, Pramod K. Subbareddy, and Graham V. Candler. Simulation of Boundary Layer Transition on Elliptic Cones in Hypersonic Flow. AIAA Paper 2010-1064, January 2010.

[53] Chau-Lyan Chang, Meelan M. Choudhari, and Fei Li. Numerical Computations of Hypersonic Boundary-Layer over Surface Irregularities. AIAA Paper 2010-1572, January 2010.

[54] D. C. Reda, M. C. Wilder, and D. K. Prabhu. Transition Experiments on Blunt Bodies with Isolated Roughness Elements in Hypersonic Free Flight. AIAA Paper 2010-1367, January 2010.

[55] P. S. Klebanoff and K. D. Tidstrom. Mechanism by Which a Two-Dimensional Roughness Element Induces Boundary-Layer Transition. *The Physics of Fluids*, 15(7):1173–1188, July 1972.

[56] Bradley M. Wheaton. Roughness-Induced Instability in a Laminar Boundary Layer at Mach 6. Master's thesis, Purdue University School of Aeronautics & Astronautics, West Lafayette, IN, December 2009.

[57] E. R. Van Driest and W. D. McCauley. The Effect of Controlled Three-Dimensional Roughness on Boundary-Layer Transition at Supersonic Speeds. *Journal of the Aerospace Sciences*, 27(4):261–271,303, April 1960.

[58] Bradley M. Wheaton and Steven P. Schneider. Roughness-Induced Instability in a Laminar Boundary Layer at Mach 6. AIAA Paper 2010-1574, January 2010.

Appendix A

Viscous Flux via Gradient Reconstruction

In one dimension the viscous fluxes, using deferred correction, do not consider the gradients in the left and right cells. Instead the difference across the face is used as the gradient at the face. If, however, the gradients are combined with the difference across the face a larger stencil can be achieved with the correct fourth order representation.

$$\phi_{x,i+\frac{1}{2}} = \alpha \left(\frac{\phi_{x,i} + \phi_{x,i+1}}{2} \right) + \beta \left(\frac{\phi_{i+1} - \phi_i}{\Delta x} \right) \tag{A.1}$$

where α and β are introduced as parameters to be determined. Knowing that the gradients in the left and right cells are second order accurate, equation A.1 can be expanded and arranged in the following way.

$$\phi_{x,i+\frac{1}{2}} = \frac{-\alpha\ \phi_{i-1} - (\alpha + 4\beta)\ \phi_i + (\alpha + 4\beta)\ \phi_{i+1} + \alpha\ \phi_{i+2}}{4\Delta x} \tag{A.2}$$

Also, it is known that to get the correct fourth order accurate second derivative at the cell center, the derivative at the face must be

$$\phi_{x,i+\frac{1}{2}} = \frac{\phi_{i-1} - 30\phi_i + 30\phi_{i+1} - \phi_{i+2}}{12\Delta x} \tag{A.3}$$

Equating coefficients finds that for $\alpha = -1/3$ and $\beta = 4/3$ a formally fourth order second derivative is obtained. Following the method used for the inviscid fluxes, if a hexahedral grid is being used, then it is possible to use connectivity to obtain the cells one level further from a face than just the left and right cells. Then, using this larger stencil it is possible to get a sixth order scheme. Writing the gradient at the face as

$$\phi_{x,i+\frac{1}{2}} = \alpha \left(\frac{\phi_{x,i} + \phi_{x,i+1}}{2} \right) + \beta \left(\frac{\phi_{x,i-1} + \phi_{x,i+2}}{2} \right) + \gamma \left(\frac{\phi_{i+1} - \phi_i}{\Delta x} \right) \tag{A.4}$$

it is possible to rearrange it as

$$\phi_{x,i+\frac{1}{2}} = \frac{-\beta\ \phi_{i-2} - \alpha\ \phi_{i-1} - (\alpha - \beta + 4\gamma)\ \phi_i + (\alpha - \beta + 4\gamma)\ \phi_{i+1} + \alpha\ \phi_{i+2} + \beta\ \phi_{i+3}}{4\Delta x} \tag{A.5}$$

Again, to get the correct sixth order accurate second derivative at the cell center, the derivative at the face must be

$$\phi_{x,i+\frac{1}{2}} = \frac{-2\phi_{i-2} + 25\phi_{i-1} - 245\phi_i + 245\phi_{i+1} - 25\phi_{i+2} + 2\phi_{i+3}}{180\Delta x} \tag{A.6}$$

Equating coefficients results in $\alpha = -5/9$, $\beta = 2/45$ and $\gamma = 68/45$.

In higher dimensions there are cross-terms that must be considered. For a two-dimensional Cartesian grid, for example, the term $\left(\frac{\partial u}{\partial y}\right)_{i+\frac{1}{2},j}$ must be accounted for. In these cases, the ability to extend the stencil using gradients is very limited. In fact, any direction perpendicular to the face normal has the problem of only being able to obtain a stencil directly accessible in memory. The result of summing the fluxes for this term would be the $\left(\frac{\partial^2 u}{\partial x \partial y}\right)_{i,j} + \mathcal{O}(\Delta x^2, \Delta y^2)$ if the left and right neighbors are simply averaged. It is possible to use the one extra cell to the left and right that are known.

$$\left.\frac{\partial u}{\partial y}\right|_{i+\frac{1}{2},j} = \frac{\alpha}{2}\left(\left.\frac{\partial u}{\partial y}\right|_{i,j} + \left.\frac{\partial u}{\partial y}\right|_{i+1,j}\right) + \frac{\beta}{2}\left(\left.\frac{\partial u}{\partial y}\right|_{i-1,j} + \left.\frac{\partial u}{\partial y}\right|_{i+2,j}\right) \tag{A.7}$$

By choosing $\alpha = 7/6$ and $\beta = -1/6$ the order of accuracy of the term can be slightly improved to $\left(\frac{\partial^2 u}{\partial x \partial y}\right)_{i,j} + \mathcal{O}(\Delta x^4, \Delta y^2)$.

In practice, it seems an approach similar to deferred correction can be used. The component of the gradient in the direction of the face normal can be made sixth order. The component normal to the face normal will be lower order.